Schuscha *et al. J. Mater. Inf.* **2025**, *5*, 28
DOI: 10.20517/jmi.2024.90

Journal of materials Informatics

Research Article

Open Access

Uncertainty aware design space modeling for sample efficiency in material design of bainitic steels

Bernd Schuscha[1,#,*], Sophie Steger[2,#], Franz Pernkopf[2], Dominik Brandl[1], Lorenz Romaner[3], Daniel Scheiber[1]

[1]Materials Center Leoben Forschungs GmbH, Leoben 8700, Austria.
[2]Institute of Signal Processing and Speech Communication, Graz University of Technology, Graz 8010, Austria.
[3]Department of Materials Science, Montanuniversität Leoben, Leoben 8700, Austria.

[*]**Correspondence to:** Bernd Schuscha, Materials Center Leoben Forschungs GmbH, Roseggerstraße 12, Leoben 8700, Austria. E-mail: bernd.schuscha@mcl.at; Sophie Steger, Institute of Signal Processing and Speech Communication, Graz University of Tech-nology, Inffeldgasse 16C, Graz 8010, Austria, E-mail: sophie.steger@tugraz.at

How to cite this article: Schuscha, B.; Steger, S.; Pernkopf, F.; Brandl, D.; Romaner, L.; Scheiber, D. Uncertainty aware design space modeling for sample efficiency in material design of bainitic steels. *J. Mater. Inf.* **2025**, *5*, 28. http://dx.doi.org/10.20517/jmi.2024.90

Received: 20 Dec 2024 **First Decision:** 24 Jan 2025 **Revised:** 14 Feb 2025 **Accepted:** 24 Feb 2025 **Published:** 24 Mar 2025

Academic Editor: Xiang-Dong Ding **Copy Editor:** Pei-Yun Wang **Production Editor:** Pei-Yun Wang

Abstract

Optimizing sampling efficiency is crucial for solving complex material design challenges, especially with a limited experimental budget. This study focuses on improving sampling efficiency by reducing the search space for carbide-free bainitic steels through the uncertainty-aware modeling of constraints. These constraints include avoiding the formation of undesirable competing phases such as carbides, ferrite, and martensite, as well as accounting for practical limitations on phase transformation durations. Experimental data, obtained through dilatometry and metallography, inform most constraints, except for the presence of carbides. To model these constraints, we use machine learning (ML) models trained on a combination of newly acquired experimental data and experimental data from the literature. Predicting properties in unexplored regions of the design space can lead to inaccuracies. Thus, reliable uncertainty quantification is essential to avoid excluding parts of the design space due to overconfident erroneous predictions. To address this, we employ conformal prediction (CP), a distribution-free framework that provides calibrated post-hoc uncertainty estimates for the different ML models, ensuring reliable extrapolations without prematurely excluding viable design regions. This approach achieves a reduction ranging from 80% to more than 99% depending on the strictness of the employed criteria reduction in the search space, greatly enhancing sampling efficiency without compromising reliability.

Keywords: Uncertainty, machine learning, conformal prediction, bainite

INTRODUCTION

Iterative optimization loops, such as Bayesian optimization, are an effective tool for material discovery and property optimization[1]. These approaches rely on surrogate models as computationally efficient approximations of the true objective function. Since evaluating the true objective requires costly experiments, surrogate models facilitate property estimation in the design space by using prior knowledge and experimental data[2–7]. With each iteration, newly acquired data refines the approximation of the surrogate model, enabling more informed sampling[1]. The search space, often represented as a hypercube, includes all possible input configurations considered during optimization. It is a crude approximation of the true design space, which is an optimized subset of configurations that meet specific criteria and constraints set by the design objectives.

In steel, different microstructures can form despite having the same chemical composition by varying process parameters, such as heat treatment. Depending on the microstructure, diverse mechanisms may govern the same property, resulting in multiple process-microstructure-property relationships[8,9]. For this reason, steels are classified into different types[10]. Beyond that, when multiple microstructures coexist, their properties mostly do not exhibit simple additive behavior[11–13], creating significant modeling challenges, which can lead to poor generalization abilities of models. In material design, especially when using methods that rely on model predictions, such as Bayesian optimization, this can lead to sampling in uninformative or practically infeasible regions, reducing optimization efficiency and wasting resources. To address this, a preselection of a steel type is necessary, allowing models to generalize property predictions more effectively.

In the present work, we focus on carbide-free bainitic (CFB) steel, a promising and cost-effective type of advanced high-strength steel. Its microstructure is primarily composed of bainitic ferrite and retained austenite, with minimal carbide content[14]. Rather than optimizing for specific properties, this work focuses on classifying points within the search space as either CFB or non-CFB. Additionally, we incorporate constraints based on industrial manufacturing requirements, in particular, the bainitic phase transformation time. These constraints lead to non-trivial boundaries of the design space[15], within which chemical compositions and heat treatment parameters can be optimized for desired properties. This ensures that Bayesian optimization focuses exclusively on industrially feasible samples that lead to valid CFB steels. Some methods actively model the valid design space either during[16] or before optimization[6]. However, these approaches often rely on the intentional generation of non-valid samples to refine boundary definitions, which can be resource-intensive. In our work, we model the individual physical processes required to produce CFB steel, breaking down the overall classification problem (CFB *vs.* non-CFB steel) into simpler sub-problems. This modular approach facilitates the integration of domain-specific knowledge or physics and enables more effective use of experimental data. For instance, a prerequisite for achieving CFB steel is a complete transformation to austenite without the formation of carbide or ferrite. This constraint can be modeled independently of subsequent processing steps, enabling the use of physical models or literature data unrelated to bainitic steel.

As the availability of accurate physical models is limited for the given problems, we use machine learning (ML) models to predict the constraints from experimental data produced in the present work and from the literature. However, ML models often perform poorly when the distribution of the training data differs from that encountered during testing or deployment (e.g., novel material compositions or processing parameters). This is referred to as distribution shifts[17,18] and requires the model to extrapolate. In such cases, learned correlations of the model from the training data may no longer hold, leading to inaccurate predictions. One approach to addressing this issue is to improve model generalization and extrapolation capabilities by incorporating physical knowledge, although this can be challenging and is not always feasible[19]. Alternatively, distribution shifts can be detected, and the confidence levels of predictions can be adjusted accordingly to account for uncertainty. By providing uncertainty estimates, we mitigate the risk of incorrect decisions resulting from overconfident, erroneous predictions by ML models. In our application, this ensures that potentially valuable material compositions, for which the ML models are uncertain or unreliable, are not prematurely discarded.

Uncertainty estimates in practical applications often suffer from calibration issues - this refers to a mismatch between the predicted uncertainty intervals and the actual probability that the true value falls within those intervals[20]. For example, if a model predicts a 90% confidence interval, but the true value only falls within the interval 70% of the time, the model is considered poorly calibrated. This undermines the reliability of predictions and can lead to suboptimal decisions. To address this, we employ conformal prediction (CP)[21,22], a distribution-free method that calibrates uncertainty estimates to guarantee valid prediction intervals with specified coverage probabilities. To further increase robustness regarding distribution shifts, we extend this approach with distance-aware uncertainty estimates[23]. By incorporating a distance metric between the test data points and the training data, we assign higher uncertainty scores to test points that are far away from our training set.

Using this framework, we evaluate the performance of various ML models - including Gaussian processes regression, random forests (RFs), gradient boosting machines, linear and polynomial regression, neural networks (NNs), and support vector machines (SVM)- for predicting the aforementioned constraints. The models are compared in terms of predictions and prediction intervals. To the best of our knowledge, no prior work has emphasized the importance of addressing distributional uncertainty arising from distribution shifts in the Bayesian optimization for material discovery of material compositions and process parameters. For a confidence level of 90%, the search space can be reduced by 80%.

Importantly, this method serves as a versatile extension to any predictor within the Bayesian optimization framework, offering uncertainty estimates that are more robust to distributional shifts.

MATERIALS AND METHODS

Design problem

In the present work, we are modeling the design space of CFB steels. In this steel type, the carbide precipitation is suppressed during bainitic transformation by adding silicon[24] or aluminum[25,26], and it is defined as having at least 1 wt.% silicon. The retained austenite is stabilized by carbon, which is redistributed during the bainitic transformation from bainitic ferrite to retained austenite[14]. We place a lower limit of carbon concentration to ensure some retained austenite. Additionally, considered alloying elements are Si, Mn, Cr, Mo, Al and V, excluding critical raw elements such as Ni, W and Co [Table 1]. Furthermore, CFB steel is intended to exhibit relatively low overall alloying content. Therefore, the total concentration of alloying elements, denoted as $\sum_{\mathrm{wt.\%}}$, is restricted to a maximum of 10 wt.%. We decided to focus on two representative processes: isothermal holding or austempering which is shown in Figure 1A and continuous cooling which is shown in Figure 1B.

As illustrated schematically, the sample is heated up to an austenitization temperature, typically above 800 °C and held for a duration t_A to obtain the high-temperature phase of steel, austenite (A). Subsequently, the sample is either rapidly and continuously cooled to an isothermal holding temperature T_iso or continuously cooled directly to room temperature with a cooling rate $\dot{T}$ to obtain ferrite/Pearlite (F/P), bainite (B), martensite (M) microstructures or a mixture of both. Both processes have an upper time limit: the isothermal process is limited by a maximum holding time $\max(t_\mathrm{iso})$, while the continuous cooling process is limited by a maximum cooling rate $\max(\dot{T})$. This defines the search space in the present work, which is summarized in Table 1.

The requirement for the sample to be only bainitic (B) can be expressed by a list of constraints, which are listed below and, if applied to the search space, yield the design space. As can be seen in Figure 1, both processes have windows for the process parameters, which are composition-dependent.

Table 1. Search space

	C	Si	Mn	Cr	Al	V	Mo	$\Sigma_{wt.\%}$	T_{iso}	$\dot{T}$
Unit	wt.%	wt.%	wt.%	wt.%	wt.%	wt.%	wt.%	wt.%	°C	°C/s
Min	0.2	1	0	0	0	0	0	1.2	250	0.1
Max	1	4	4	4	4	0.5	4	10	600	25

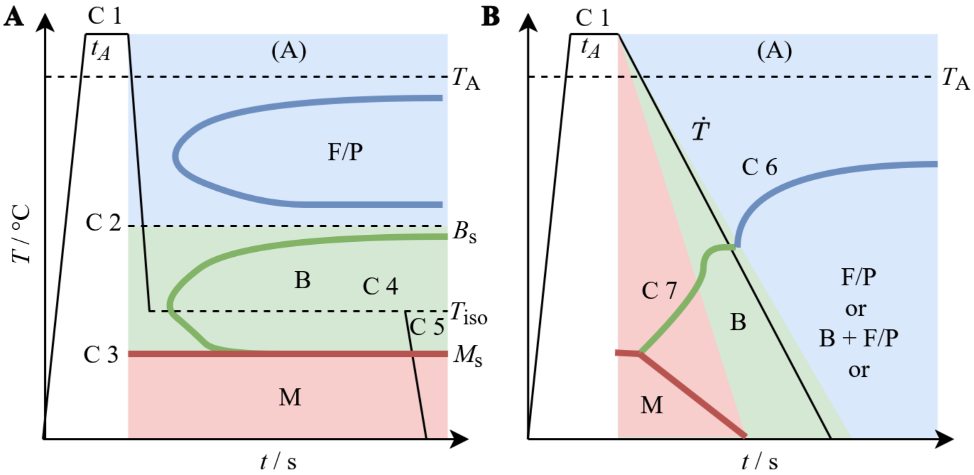

Figure 1. Temperature profile (in black) for the processes leading to the formation of CFB, along with time/temperature regions where constraints apply: (A) isothermal holding (austempering) and (B) continuous cooling. Colored regions indicate phases: Ferrite/Pearlite (F/P), Bainite (B), and Martensite (M). The constraints are enumerated by C1-C7. CFB: Carbide-free bainite.

C1 - Homogeneity of austenitization

For the present modeling approach of CFB steels, a complete transformation to the austenite phase without the formation of additional phases such as carbides or ferrite is necessary. This can be expressed as

$$\exists\, T_A \in \mathbb{R} \qquad \text{such that} \qquad f_{\text{austenite}}(T_A) = 1\,, \tag{1}$$

where $f_{\text{austenite}}$ is the austenite phase fraction. To fulfill this requirement, it must be ensured that ferrite-stabilizing elements such as chromium or molybdenum do not stabilize ferrite up to the melting temperature and carbide forming elements do not stabilize carbides. Extensive data on the occurrence of carbides, austenite, and ferrite is encoded in thermodynamic databases with the CALPHAD approach[27,28], which will be used for this constraint. However, predictions from CALPHAD databases are not without limitations. To account for uncertainties, it is common practice to include a safety margin of 50 °C. Applying this margin to both the upper and lower bounds of a temperature range results in an effective window of 100 °C. For practical applications, this temperature window should lie between 800 and 1,200 °C, resulting in the constraint

$$\exists\, T_A \in [800, 1200] \qquad \text{such that} \qquad f_{\text{austenite}}(T) = 1 \qquad \forall\, T \in [T_A - 50, T_A + 50]\,. \tag{2}$$

This constraint is implicitly fulfilled in most works considering CFB steels.

C2 - Bainite start temperature

The occurrence of bainite is limited by a maximum temperature, the bainite start temperature B_S. This can be formulated as

$$T_{\text{iso}} < B_S(w_{C,0}, \{w\})\,, \tag{3}$$

with $w_{C,0}$ as the initial carbon concentration of the alloy and $w = \{w_{\text{Si}}, w_{\text{Mn}}, w_{\text{Cr}}, w_{\text{Mo}}, ...\}$ as the concentrations of the other alloying elements. For the isothermal process, this is the upper bound of the temperature range. The bainite start temperature is modeled either by data-driven[29,30] or by physical models based on different theories[14,31,32]. However, it was found that there is no significant difference between a linear regression model and more physically based approaches[31]. For this reason, different ML models are tested in this work.

C3 - Martensite start temperature of the initial alloy

The martensite start temperature is the lower limit of the process window for the isothermal process. This boundary is given by

$$T_{\text{iso}} > M_S(x_{C,0}, \{x\}_i)\,. \tag{4}$$

There are a multitude of models for the martensite start temperature available in literature based on ML and thermodynamic modeling[29,33] with reasonable prediction accuracy. However, none of them are provided in an executable form and ready to use out of the box.

C4 - Bainite transformation time

Depending on the chemical composition ($x_{C,0}, \{x\}_i$) and the isothermal holding temperature T_{iso}, the transformation time for the bainitic phase transformation can vary by several orders of magnitude, ranging from seconds to weeks. To ensure that the transformation is nearly complete, we have chosen the time required to achieve 90% of the transformation as the basis for the time constraint in Table 2. This can be expressed as

$$t_{90\%}(w_{C,0}, \{w\}, T_{\text{iso}}) < 10800\ \text{s} \quad (3\ \text{h})\,. \tag{5}$$

Several works have attempted to predict this property using purely data-driven, phenomenological, or physics-based models[34–38], but with little to no extrapolative prediction quality and none that are ready to use out of the box.

C5 - Martensite start of retained austenite for the isothermal case

The martensite start temperature is the same phenomenon as in constraint C3, but for the retained (=remaining) austenite after the bainitic phase transformation. During this transformation, the retained austenite is enriched with carbon, which lowers its martensite start temperature. This can be expressed as

$$M_{S,RA}(w_C(T_{\text{iso}}), \{w\}) < 25\ ^\circ\text{C}\ , \tag{6}$$

where $w_C(T_{\text{iso}})$ is the carbon concentration after a bainitic transformation. It is based on the same models as the martensite start temperature of the initial alloy, but a redistribution of carbon during the bainitic transformation has to be considered. This can be modeled using the T_0 concept[14].

C6 - Critical cooling rate of ferrite and pearlite

The critical cooling rate is the lowest cooling rate at which F/P can occur. It is determined from a continuous cooling transformation (CCT) diagram.

$$\dot{T} > \dot{T}_{\text{crit}}(x_{C,0}, \{x\}_i) \tag{7}$$

When designing new steels, it provides information about the process windows. There have been efforts to predict the occurrence of phases during continuous cooling, either with regression[34,35] or other ML methods[36–38].

C7 - Martensite start of retained austenite for the continuous cooled case

Constraint C7 represents the martensite start temperature of retained austenite in the continuous cooling process. Modeling this would require predicting the kinetics of carbide-free bainite formation and the redistribution of carbon in retained austenite as functions of the cooling rate. Currently, there is neither a suitable predictive model nor sufficient data available to address this, and hence it was excluded from this work. As a result, the predictions in this study do not account for a maximum cooling rate, which will result in an overestimation of the design space size for continuously cooled carbide-free bainite.

Data generation for C1 - homogeneity of austenitization

The stability and occurrence of carbides, austenite, and ferrite phase is modeled in thermodynamic databases. The MatCalc Software[28] and database (mc_fe version 2.061[39]) are used to calculate equilibrium temperature scans for a surrogate model to increase in evaluation speed. The MatCalc simulation considers the following phases in the scan for the austenitization temperature: liquid, austenite, ferrite, cementite, and several other carbides (M6C, M7C3, M23C6, LAVES_Phase, K_CARB, and FCC_A1#01). For each alloy composition, a temperature scan of equilibrium calculations is performed starting at a temperature of 1,873 °C and a step size of 2 °C.

Evaluation of carbon redistribution for C4

For a given isothermal holding temperature (T), the retained austenite during bainitic transformation is enriched with carbon until a maximum $w_C(T)$, at which point the driving force for the transformation is completely consumed. This can be interpreted as the bainite start temperature of the alloy with the enriched carbon concentration

$$w_C : T = Bs(w_C(T), \{w\}) . \tag{8}$$

The carbon enrichment of the retained austenite stabilizes it against martensite transformation during cooling to room temperature. This explains the difference between the martensite start of the initial alloy $M_S(w_{C,0}, \{w\})$ and of the retained austenite $M_{S,RA}(w_C(T), \{x\})$. Both are modeled similarly, but for the retained austenite, the carbon enrichment $w_C(T)$ must be predicted. This can be done with a bainite start model (C2), but the model is strongly extrapolated for carbon concentrations. Therefore, the best-performing physical-based displacive bainite start model from Ref.[31] paired with the mc_fe version 2.061 database[39] is used for the prediction.

Experimental data

The data used in this work consists of experimental data from literature, as well as experimental data produced in this work. The experimental details for the production of the samples are described in Ref.[31]. The alloys were fabricated using a high-frequency remelting furnace (HRF), the "PlatiCast-600-Vac," from the Linn High Therm GmbH, Germany[40,41]. Approximately 450 g of each alloy, shaped into 26.5 mm × 26.5 mm × 90 mm ingots, was melted using high-purity raw materials. The process took place in a pure alumina crucible under an argon atmosphere at five atmospheres overpressure. The molten material was centrifugally cast into a cold copper mold, resulting in highly homogeneous samples due to the combination of inductive melting, centrifugal casting, and rapid solidification.

Chemical composition analyses, detailed in Table 2, are performed using optical emission spectroscopy (OES, model OBLF QSG 750). To ensure a consistent initial microstructure, the raw samples underwent heat treatment in an argon-purged chamber furnace. This included diffusion annealing at 1,200 °C for four hours, achieved with a heating rate of 300 °C/s. Following this, the samples were removed from the furnace and allowed to cool freely to room temperature. To further refine the coarse-grained microstructure, a normalization annealing was conducted at 960 °C - at least 50 °C above the previously calculated Ae3 temperature - for 50 min, followed by free cooling to room temperature. Metallographic examination of the resulting ingots confirmed a uniform microstructure.

Cylindrical dilatometer samples with a diameter of 4 mm and a length of 10 mm are produced. The heat treatment and measurement is done with a TA Instruments DIL 805 A dilatometer in vacuum. The samples are austenitized for 30 min at 960 °C with a heating rate of 2 K/s. The bainite start temperature was measured for selected compositions, with the methods described in Ref.[31]. The region of carbide free bainitic steels was determined with various isothermal and continuous cooled experiments by observing the region of ferrite/pearlite and martensite.

The evaluation of the martensite start temperature of the initial alloy, the martensite start temperature of the re-

Table 2. Composition of all alloying elements in wt.% of model alloys

Name	C	Si	Mn	Cr	Mo	Al	V
S1	0.21	1.64	0.87	1.19	0.64	0.03	0.11
S2	0.30	1.65	0.88	1.18	0.67	0.03	0.11
S3	0.41	1.66	0.88	1.21	0.67	0.03	0.11
S4	0.52	1.71	0.91	1.22	0.69	0.04	0.11
S5	0.60	1.65	0.88	1.19	0.67	0.03	0.11
S6	0.39	3.09	0.92	1.24	0.69	0.03	0.10
S7	0.39	1.5	1.94	0.52	0.67	0.03	0.10
S8	0.38	1.15	0.90	1.19	0.67	0.03	0.11
S9	0.82	1.37	0.31	0.01	0.56	0.84	0.00
S10	0.45	2.99	0.23	0.12	1.86	0.03	0.02
S11	0.65	1.83	0.38	0.29	1.56	0.02	0.01
S12	0.41	1.52	0.91	1.21	0.67	0.09	0.48
S13	0.69	2.59	0.65	0.59	0.00	0.01	0.00
S14	0.39	1.52	3.39	0.53	0.73	0.01	0.09
S15	0.69	3.03	1.02	0.12	0.84	2.01	0.00
S16	0.73	3.25	1.36	0.00	0.45	1.91	0.00
S17	1.05	1.58	2.47	0.04	0.65	1.24	0.04
S18	1.11	1.69	2.58	0.09	0.01	2.42	0.00
S19	0.70	3.86	1.99	0.04	0.05	1.22	0.02
S20	0.57	3.99	1.16	0.02	0.86	1.30	0.00
S21	0.70	0.00	0.63	0.59	0.00	2.59	0.00

Table 3. List of employed ML models

Task	Models
Classification	Logistic regression; RF; XGBoost; SVM; NN
Regression - local	GPR (RBF kernel); RF; LGBM
Regression - global	Linear regression; polynomial regression; NN; monotone NN; GPR (RBF kernel + LM); GPR (polynomial kernel);

ML: Machine learning; RF: random forest; SVM: support vector machine; NN: neural network; GPR: Gaussian process regres-sion; RBF: LGBM: light gradient boosting machine.

tained austenite phase and the occurrence of the F/P phase is done with the tangent method[42] and supported by metallography.

ML models

The ML models used in this work include Gaussian process regression (GPR)[43,44], linear regression, polynomial regression, logistic regression, RFs[45], gradient boosting machines [XGBoost, light gradient boosting machine (LGBM)][46,47], NNs[48], monotone NNs[49], and SVM[50]. A full list can be seen in Table 3. There are fundamentally two types of models: local models, which predict the target based on its proximity to neighboring data points, and global models, which capture overarching trends in the data.

Each of the constraints (C1 to C6) corresponds to a classification problem, where the task is to determine whether the input sample should be accepted or rejected. However, the way experimental data is reported in the literature, combined with the nature of the experiments producing this data, results in a significant class imbalance. For example, more data points are reported with a transformation time of less than three hours than with a time greater than three hours, due to the high cost of the experiments. Thus, we use regression models to predict continuous values for constraints C2 to C6, which are then thresholded to classify the samples into binary categories (accept/reject).

Except for C1, where data is sampled from a thermodynamic model, no physics-based models for the remaining constraints significantly outperform ML approaches. Since this work evaluates points across the entire search space defined in Table 2, the model operates in an extrapolative regime, which presents challenges in

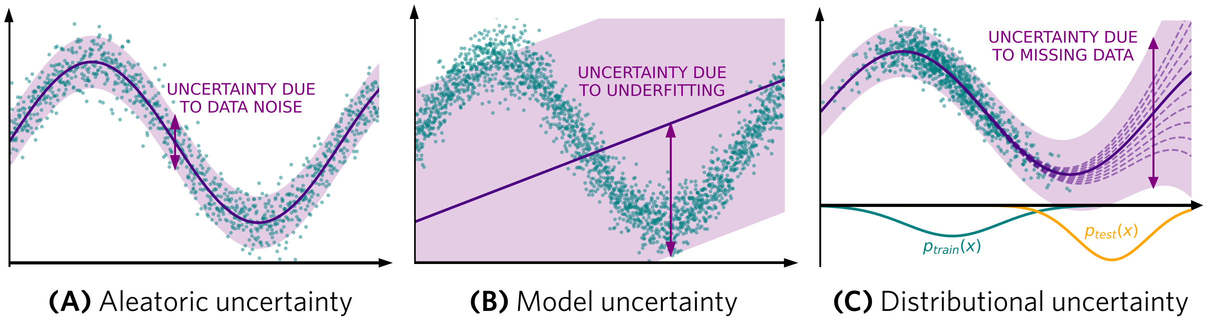

Figure 2. Illustrations of different types of uncertainty in model predictions.

ensuring reliable predictions beyond the training domain. For constraints C2 to C5, we assume that the quantities follow (at least approximately) a general trend and exhibit monotonicity. For example, if an alloy with 2 wt.% Mn fails to satisfy constraint C4, increasing Mn to 4 wt.% is also assumed to fail C4. This highlights a key challenge for local models, which may struggle to capture such trends in regions with sparse data or when extrapolating beyond the training domain. As a result, global models are better suited for addressing these constraints.

Another issue is the substantial degree of extrapolation required by the models, potentially resulting in inaccurate predictions. Thus, we also require reliable uncertainty estimation to avoid premature exclusion of valid samples. Popular methods for uncertainty estimation include probabilistic and Bayesian approaches (e.g., GPR). One advantage of GPRs with appropriate kernel functions is their ability to express a relationship between distance from the training data and uncertainty[51]. In GPR, predictions take the form of a Gaussian distribution $\mathcal{N}(\mu(x), \sigma^2(x))$, with $\mu(x)$ representing the mean prediction and $\sigma^2(x)$ denoting the variance. We use the standard deviation $\sigma(x)$ as an uncertainty measure, i.e., $u(x) = \sigma(x)$. However, GPR uncertainty estimates are reliable *only if* the model is well specified[20]. This means the chosen kernel, likelihood function, and hyperparameters must align with the true data-generating process. For example, if the kernel fails to match the actual smoothness of the data, the resulting uncertainty estimates become unreliable. Unfortunately, this condition is rarely met in practice, requiring additional calibration through CP[20,22]. In contrast, deterministic algorithms (e.g., RFs, NNs) approximate the training data as $\hat{y} = f(x; \theta)$. They scale efficiently with large datasets and can deliver competitive predictive accuracy. However, they tend to perform poorly in extrapolated regions and lack principled mechanisms for estimating uncertainty. To address this, we assume a uniform uncertainty of $u(x) = 1$ for the full input space, which is then calibrated with CP[22].

Uncertainty quantification

In this section, we summarize key sources of uncertainty and how CP provides calibrated uncertainty estimates for both probabilistic and deterministic models. Additionally, we augment the uncertainties with distance measures, e.g., Mahalanobis distance, to detect distribution shifts between the training data and data encountered during deployment. This allows us to adjust uncertainty estimates in extrapolated regions. By doing so, the uncertainty estimates are based on the proximity of the current input to the training data. This adaptation is especially useful for deterministic models, where we initially assume constant uncertainty.

Prediction uncertainties can arise from several sources[52,53], each representing a distinct type of uncertainty, as illustrated in Figure 2. Figure 2A stems from the inherent variability or noise in the data. This uncertainty is caused by random variations or measurement uncertainties, as shown by the scattered data points around the true function. In contrast, Figure 2B originates from the model's limited understanding of the data-generating process, e.g., when the model is underfitting the data and is unable to capture the complexity of the underlying function. Additionally, Figure 2C occurs when there is a mismatch between training and test distributions,

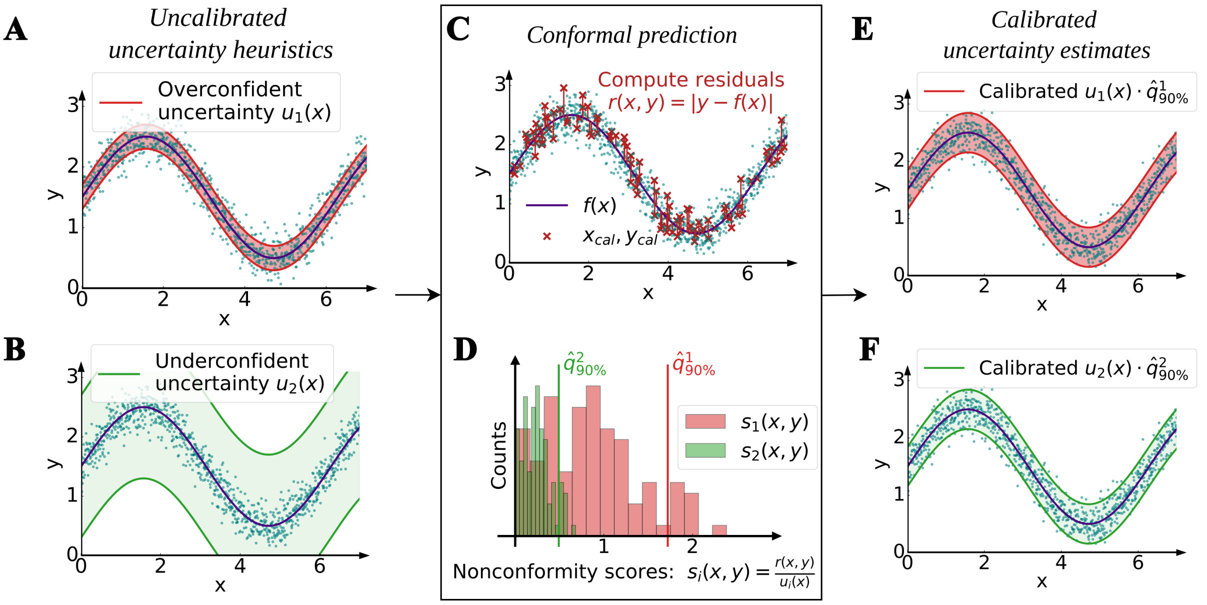

Figure 3. Calibration of uncertainty estimates using CP. Overconfident (A) and underconfident (B) prediction intervals are scaled with the split CP framework (C and D) to achieve a specified coverage with tight bounds (E and F). CP: Conformal prediction.

e.g., when certain regions of the input space are sparsely sampled or fall outside the range of the training data (i.e., extrapolation regions). In such cases, the model exhibits higher uncertainty in underrepresented areas, reflecting its limited knowledge. Accounting for this uncertainty is crucial to prevent overconfident predictions in unexplored regions of the design space, which are underrepresented in the training data. Failure to address this issue may lead to the premature exclusion of potentially valuable compositions. In the following, we describe our proposed method to account for such sources of uncertainty.

To quantify prediction uncertainty, we employ prediction intervals, which define the range within which the true value is expected to fall with a specified probability, α. Consider the training data $(x_i, y_i) \in \mathcal{D}$ for $i = 1, \ldots, n$, where x_i represents the input features and y_i the target values. Given a confidence level α, the prediction interval C_α for a new input x^* is defined by

$$\mathbb{P}[y^* \in C_\alpha(x^*)] = \alpha. \tag{9}$$

Uncertainty quantification methods often fail to guarantee such calibrated prediction intervals, i.e., intervals that reliably contain the true value with the stated probability[54]. Even GPR, an established probabilistic method for uncertainty estimation, produces uncalibrated prediction intervals in practice due to model misspecification[20,55].

CP

CP[21,22,56] calibrates prediction intervals from an uncertainty heuristic $u(x)$ (e.g., predictive variance from a GPR), making no assumptions about the underlying data distribution. CP provides prediction intervals with a user-specified coverage probability (cov) (e.g., 90%), given that the data satisfies the assumption of exchangeability. Exchangeable data means that the order of the data points does not affect their joint distribution. In simpler terms, exchangeability assumes that the data points are drawn from the same process and treated symmetrically, without requiring the stricter independent and identically distributed (i.i.d.) assumption.

To illustrate the CP workflow, Figure 3 compares two uncalibrated uncertainty heuristics, the calibration process through CP, and the resulting calibrated uncertainty estimates. Figure 3A shows overconfident estimates

$u_1(x)$, where intervals are too narrow and fail to capture the variability of the data, underestimating the uncertainty. On the other hand, the uncertainty estimates $u_2(x)$ in Figure 3B are underconfident. The intervals are excessively wide, leading to overestimation of uncertainty. Both cases highlight the need for calibration to achieve intervals that accurately reflect the desired coverage. The key idea of CP calibration is to scale the uncertainty heuristic scores of the unseen test data by a calibration factor $\hat{q}$ to obtain the prediction intervals. The calibration factor $\hat{q}$ in our example is chosen such that the prediction intervals have a cov of $\alpha = 90\%$. Due to its efficiency and simplicity, the most commonly used CP method in practice is split CP[57]. This approach divides the data into a proper training set and a calibration set. In the following, we outline the steps for implementing split CP[22].

1. We select an uncertainty heuristic $u(x)$ [e.g., GPR standard deviation $\sigma(x)$, or uniform $u(x) = 1$].
2. Next, we calculate the deviation between the model's predictions and the true observed values on a separate calibration set. For regression tasks, we compute residuals $r(x_i, y_i) = |y_i - f(x_i)|$, with $f(x_i)$ representing the model's prediction for input x_i. This results in the non-conformity scores $s(x_i, y_i) = \frac{r(x_i,y_i)}{u(x_i)}$. For classification tasks, we use the predicted probabilities for each class c, denoted as $\hat{p}_c(x_i)$. The non-conformity score is the predicted probability for the correct label y, $s(x_i, y_i) = \hat{p}_{y_i}(x_i)$.
3. We compute the calibration factor $\hat{q}_\alpha$ as the $\frac{\lceil (m+1)\alpha \rceil}{m}$ quantile of the scores $s(x_i, y_i)$, where m is the number of samples in the calibration dataset.
4. For regression models, the prediction intervals are constructed as $C_\alpha(x^*) = [f(x^*) - u(x^*)\hat{q}_\alpha,\ f(x^*) + u(x^*)\hat{q}_\alpha] = [q_l, q_u]$. For classification models, the prediction set is obtained as $C_\alpha(x^*) = \{y : \hat{p}_y(x^*) \geq \hat{q}_\alpha\}$.

For $u_1(x)$, calibration adjusts the overly narrow intervals, scaling them to meet the desired 90% coverage. For $u_2(x)$, calibration scales down the excessively wide intervals, achieving the same width as those for $u_1(x)$, while maintaining valid coverage.

Extensions for distribution shifts

For the GPR, we use its predictive variance as the uncertainty heuristic $u(x)$. For deterministic models, we assume a uniform uncertainty of $u(x) = 1$. In both cases, CP addresses aleatoric and model uncertainty [Figure 2] by calibrating intervals without requiring additional model adaptations. In the simplest scenario with $u(x) = 1$, residuals are able to capture deviations caused by data noise [Figure 2A]. For uncertainty due to underfitting [Figure 2B], CP still guarantees valid coverage, though it results in larger intervals to account for the model's reduced predictive accuracy. In contrast, distributional uncertainty arising from data shifts violates the exchangeability assumption, and requires further adjustments to the framework. To increase robustness to distributional uncertainty, we adjust the uncertainty heuristic based on the distance between new data points and the training data distribution[58]. Specifically, we incorporate a distance measure $d(x^*)$ between the new evaluation point x^* and the training distribution. The uncertainty heuristic can then be adapted as

$$u'(x^*) = u(x^*) \cdot d(x^*) \tag{10}$$

where $d(x^*)$ reflects the increased uncertainty for distant data points. We analyze several methods to estimate this distance: k-nearest neighbors (kNN)[58], the likelihood of a Gaussian mixture model (GMM)[59], Wasserstein distance[60], Mahalanobis distance[61], cosine similarities[62], and likelihood ratio[23].

To handle the need for a separate calibration set in split CP, which is typically not used during model training, we employ cross CP (CCP)[21], which allows for the full dataset to be used for training. The dataset is divided into K folds, where $K - 1$ folds are used for model training and distance prediction, and the remaining fold is used for calibration. This process is repeated for each fold, with final prediction intervals obtained through averaging.

Table 4. Dataset for the constraints; for material-specific quantities, the number of materials is equal to the number of data points

Constraint	Target quantity	Additional features	Number of materials	Number of data points
C1	-	-	800,000	
C2	B_S	Co, Ni	154	
C3	M_S	Co, Cu, Ni, W	1167	
C5	$M_{S,RA}$	Co, Cu, Ni, W	1,181	1,251
C4	$t_{90\%}$	Co, Cu, Ni	55	261
C6	T_{crit}	Co, Cu, Ni, B, W	194	

Modeling workflow and metrics

The modeling workflow, illustrated in Figure 4, evaluates prediction models and distance estimators for computing the constraints (C1-C4, C6). Due to the limited size of the experimental datasets [Table 4], we adopt a 10-fold cross-validation strategy to select the optimal prediction and distance model. The dataset is split into training and test sets, with the test set used exclusively for computing performance metrics. The split is performed based on materials (same alloy compositions), ensuring that no material in the test set overlaps with the training set. For regression tasks with limited data (C2-C6), we improve cross-validation robustness by stratifying based on discretized target with five bins, ensuring a balanced representation across folds to improve model robustness and generalization. Thus, we avoid overly optimistic results by evaluating the model's ability to extrapolate to novel material compositions, rather than predicting changes driven solely by treatment temperature variations. Table 4 summarizes the number of materials, and the number of total data samples for each constraint. Each training fold is further divided into a "proper training set" and a "calibration set" used for CCP (5-folds). The prediction model is trained using the proper training set only, avoiding contamination of the calibration set used for CP.

To address prediction target variation across several orders of magnitude - such as bainite transformation times (C4) and critical cooling rates (C6) - we apply a base-10 logarithmic transformation

$$y_i = \log_{10}(y_{i,\text{data}})\,, \tag{11}$$

where $y_{i,\text{data}}$ are the original and y_i are transformed values. This transformation reduces the scale of the targets, ensuring that error metrics emphasize relative differences over absolute magnitudes.

Metrics

For classification models, we report their predictive accuracy. The performance of the regression models is evaluated using the mean absolute error (MAE) and the coefficient of determination R^2, i.e.,

$$\text{accuracy} = \frac{1}{n}\sum_{i=1}^{n} \mathbb{I}(\hat{y}_i = y_i)\,, \tag{12}$$

$$\text{MAE} = \frac{1}{n}\sum_{i=1}^{n} |y_i - \hat{y}_i|\,, \tag{13}$$

$$R^2 = 1 - \frac{\sum_{i=1}^{n}(y_i - \hat{y}_i)^2}{\sum_{i=1}^{n}(y_i - \bar{y})^2}\,, \tag{14}$$

where n is the number of samples, $\hat{y}_i$ is the predicted target, y_i is the true target, and $\bar{y}$ is the mean of the observed targets. Higher accuracy, higher R^2 values, and lower MAE indicate better predictive performance.

The quality of CP uncertainty estimates and distance models is evaluated using the cov, the average prediction

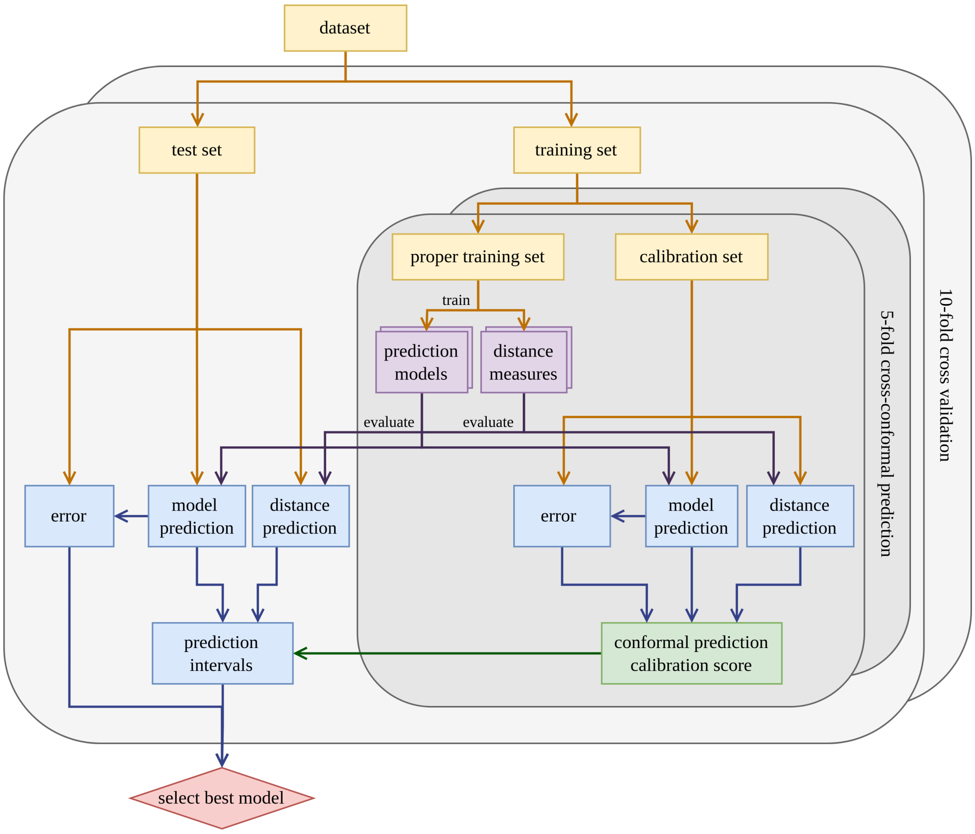

Figure 4. Overview of the model selection and evaluation process for the ML models and distance-aware cross-CP. ML: Machine learning; CP: conformal prediction.

interval width (PIW) for regression models, and the average set size for classification models, i.e.,

$$\text{cov (\%)} = \frac{1}{n}\sum_{i=1}^{n} \mathbb{I}(y_i \in C_\alpha) \times 100\,, \tag{15}$$

$$\text{PIW} = \frac{1}{n}\sum_{i=1}^{n} (q_u - q_l)\,, \tag{16}$$

$$\text{set size} = \frac{1}{n}\sum_{i=1}^{n} |C_\alpha| \tag{17}$$

where C_α is the prediction interval, q_l and q_u are the lower and upper bound of C_α, and $\mathbb{I}$ is the indicator function. The cov quantifies how often the true target falls within the predicted intervals, ideally matching the nominal level (e.g., 90%). However, excessively wide intervals can trivially achieve high coverage but lack informativeness. To balance coverage and informativeness, the distance model should increase interval widths in regions of low data density and reduce them in regions with high density.

RESULTS AND DISCUSSION

Experimental results

The combined experimental results for the sample produced in the present work are listed in Table 2 and shown in Figure 5. The experimental uncertainty for the martensite start temperature of the initial alloy is 20 °C; for the retained austenite it is 30 °C, and for the logarithmic transformation times it is 0.2 log(s). The martensite start temperature (M_S) of the initial alloy is indicated by a dashed blue line on both temperature

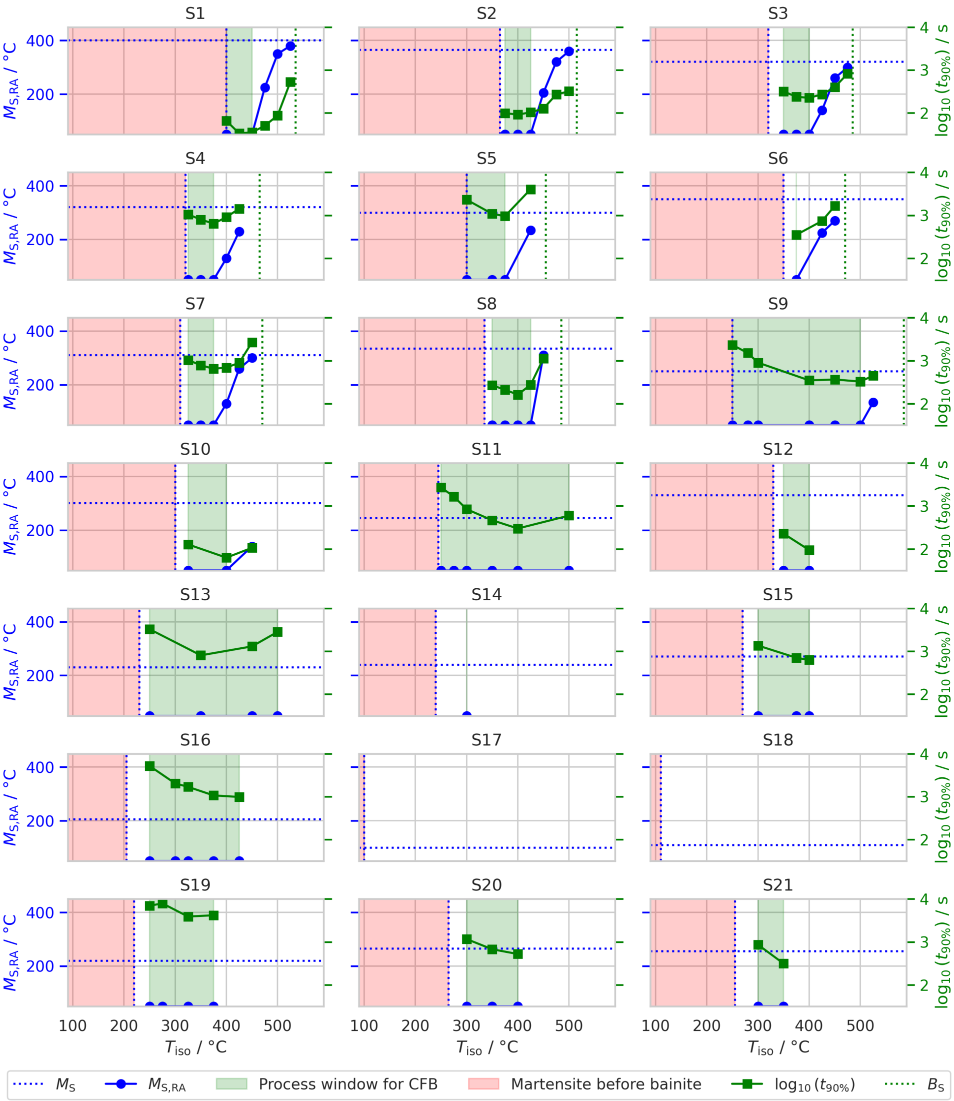

Figure 5. Experimental results for logarithmic bainitic transformation time $\log_{10}(t_{90\%})$, the martensite start temperature of the initial alloy M_S and the martensite start temperature of the retained austenite $M_{S,RA}$. For $M_{S,RA}$ under the detection limit of 50 °C, it is drawn at 50 °C. The combination of these measurements gives the process window for CFB steel, visualized with the green area. CFB: Carbide-free bainitic.

axes, serving as a reference. This temperature defines the lower limit of the isothermal holding temperature (T_{iso}), with the restricted region of T_{iso} shaded in red. On the vertical axis, the martensite start temperature of the retained austenite ($M_{S,RA}$) is shown in blue. The bainite start temperatures of the alloys, already published in Ref.[31], are indicated as green dashed lines. At the bainite start temperature (B_S), no bainite forms, resulting in $M_S = M_{S,RA}$. As the temperature decreases, carbon enrichment occurs, leading to a stabilizing effect that lowers the martensite start temperature. This decrease continues until the martensite start temperature falls below the detection limit. For consistency, these undetectable points are marked at 50 °C in Figure 5. This trend is observed across all produced samples.

The bainitic transformation time spans several orders of magnitude due to the strong influence of material composition and thermodynamic parameters on the kinetics of the phase transformation. To better illustrate this behavior, $\log_{10}(t_{90\%})$ represents the time required to achieve 90% of the bainitic transformation, which is illustrated in Figure 5. This logarithmic representation provides a clearer comparison of the transformation times across different samples.

The transformation times typically exhibit a characteristic C-shaped behavior, which can be observed in several of the samples. Samples S1 to S5, for example, were specifically designed to study the effect of varying carbon content on transformation kinetics. As shown in Figure 5, increasing the carbon content leads to a significant increase in transformation time. For samples S14, S17, and S18, the bainitic phase transformation did not complete at any isothermal holding temperature, leaving the martensite start temperature (M_S) of the initial alloy as the only usable data point. The composition of S14 is identical to that of S7, except for an increased manganese content. This difference highlights the strong influence of manganese on transformation kinetics, as its presence significantly delays the bainitic transformation. The too slow transformation kinetics of S17 and S18 can be explained by their very high carbon content of over 1 wt.%. For the remaining samples, no clear correlation between transformation time and material composition is evident.

The process window for CFB steels, highlighted in green in Figure 5, is defined by the following conditions: The isothermal holding temperature exceeding the martensite start temperature, the martensite start temperature of the retained austenite being below the detection limit, and the transformation completing within 10,800 s. The region between the red and green areas represents a high probability that the isothermal holding temperature within this range will also produce carbide-free bainite. However, this assumption has not been experimentally validated. Depending on the material composition, the process window can vary significantly: it can be quite large (e.g., for samples S9, S11, and S13) or even non-existent (e.g., for samples S14, S17 and S18).

Dataset

The primary classification task in this study is to determine whether the steel type is CFB for a given chemical composition and heat treatment parameters. However, by decomposing the problem into multiple constraints, the available data for each constraint can be expanded by incorporating data from other steel groups, assuming that the underlying physical phenomena are consistent. For instance, the formation of ferrite or pearlite is not influenced by whether or not bainite is subsequently formed. Similarly, the bainite start temperature is independent of whether the steel is bainitic or CFB.

The dataset and models utilized in this study are publicly accessible through the associated Zenodo repository (Code and datasets will be published upon acceptance). The dataset for the austenitization condition is produced with MatCalc on a grid with eight grid points for each dimension and the limits listed in Table 2. The total alloy content limit $\sum_{\text{wt.\%}}$ of 10 wt.% is enforced beforehand, which reduces the number of grid points from 8^7 one-third to about 800,000.

For the bainite start temperature, the dataset is taken from Ref.[31]. The dataset for martensite start temperatures M_S is derived from a comprehensive collection in Ref.[33] combined with experimental data from the present work. For the martensite start temperature of the retained austenite, the dataset from the normal martensite start temperature is used, combined with experimental data from the present work with adapted carbon concentration according to the description in the methods. Bainitic transformation times are obtained by digitizing bainitic phase transformation curves from the Refs.[63–80] and experimental data from the present work. The literature data for ferrite transformation times was digitized from steel transformation time atlases[81–83]. For all datasets, feature selection was performed to refine the dataset, excluding features or elements with insufficient entries or concentrations too low to have a measurable influence on the targets.

The constraints are a combination of material-specific quantities, which depend solely on composition (C1, C2, C3, C6), and process-dependent quantities (C4, C5). For the process-dependent quantities, this leads to a dataset that is sparse across most dimensions, except for temperature. To provide a clearer representation of the datasets, the number of materials, the number of data points and additional features to C, Si, Mn, Cr, Mo,

Table 5. Results for constraint C1 (homogeneity of austenitization) using ML models with 10-fold cross-validation and distance-weighted cross-CP

Metric	Logistic Regression	RF	XGBoost	SVM	<u>NN</u>
accuracy (↑)	$83.22_{\pm 0.11}$	$97.16_{\pm 0.06}$	$96.17_{\pm 0.06}$	$95.45_{\pm 0.23}$	<u>$96.90_{\pm 0.18}$</u>
cov (90%)	$90.00_{\pm 0.10}$	$90.27_{\pm 0.07}$	$94.58_{\pm 0.28}$	$89.99_{\pm 0.03}$	<u>$90.01_{\pm 0.13}$</u>
set size (↓)	$1.15_{\pm 0.00}$	$0.90_{\pm 0.00}$	$0.98_{\pm 0.00}$	$0.91_{\pm 0.00}$	<u>$0.90_{\pm 0.00}$</u>

The best model is underlined. ML: Machine learning; CP: conformal prediction; RF: random forest; SVM: support vec-tor machine; NN: neural network.

Al, V and T_{iso} for all constraints are summarized in Table 4.

Modeling results

With the datasets presented in Table 4, we assess the performance of the different ML models listed in Table 3 with 10-fold cross-validation. For each constraint, the best-performing model is selected for subsequent investigations.

The first condition C1, austenitization, is a classification task. The training data is obtained from simulations, and the ML models act as surrogate models to replace time-intensive simulations for novel input compositions. The results for the different ML models are summarized in Table 5, with NNs achieving over 97% accuracy on the test set splits, and the desired cov of 90%. Figure 6A illustrates the calibration curve and confusion matrix for NNs. The predicted probabilities closely align with the true probabilities, as indicated by the calibration curve (blue solid line) and the perfectly calibrated line (black dashed line). Additionally, the confusion matrix shows the performance of the classifier, with 63.82% of samples correctly classified as invalid, 32.28% correctly classified as valid, and minor misclassifications in the remaining categories.

For the other constraints, the training data is sourced from experimental results, introducing a higher degree of variability and uncertainty compared to purely simulation-based data as is the case for C1. Additionally, the data does not span the entire design space, requiring the models to extrapolate. To account for distribution shifts, we use distance-aware CP.

The bainite start temperature (C2), martensite start temperature (C3), and martensite start temperature of the retained austenite (C5) are grouped together as they all focus on a transition temperature. For these constraints, we assume that the problem is monotonic with respect to each alloy element. The performance of the ML regression models is listed in Tables 6-8. The test prediction performance of the best ML regression models is shown in Figure 6B-D. Green points correspond to predictions within the 90% coverage region ($C_{90\%}$), while red points indicate predictions outside this region. The dashed black line represents perfect agreement between predicted and true values. The histogram shows the distribution of prediction errors scaled by uncertainty. These models showing the best performance are used for the final evaluation on the whole design space.

When comparing the results for C2, C3 and C5, it is important to consider that we report results for local and global models shown in Table 3. However, local methods are less desirable due to their poor extrapolation behavior beyond the training data. Tree-based models (RF and LGBM) extrapolate using piecewise constant behavior in regions without training data. Also, GPR with an RBF kernel reverts back to the mean of the training data when extrapolating. Both behaviors fail to account for the physical constraints inherent in the system. For GPR with an RBF kernel, this limitation can be addressed by implementing a linear mean (LM) function, ensuring better alignment with the physical knowledge of the constraints. For the three constraints, the inclusion of quadratic features in polynomial regression has led to worse performance compared with linear regression, which can be attributed to overfitting. The coverage for all constraints and models remains

Table 6. Results for constraint C2 (bainite start temperature) using ML models with 10-fold cross-validation and distance-weighted cross-CP

Metric	Linear regression	Polynomial regression	GPR (RBF + LM)	GPR (Polynomial)	NN (Monotone)	GPR (RBF)	RF	LGBM
R^2 (↑)	$0.86_{\pm 0.03}$	$0.1_{\pm 0.5}$	$\underline{0.89_{\pm 0.04}}$	$0.85_{\pm 0.05}$	$0_{\pm 1}$	$0.87_{\pm 0.04}$	$0.7_{\pm 0.1}$	$0.7_{\pm 0.1}$
MAE (↓)	$17_{\pm 2}$	$18.0_{\pm 2.1}$	$\underline{14_{\pm 3}}$	$16_{\pm 3}$	$23_{\pm 12}$	$15_{\pm 4}$	$24_{\pm 4}$	$23_{\pm 5}$
cov (90%)	$92_{\pm 8}$	$92_{\pm 8}$	$\underline{94_{\pm 7}}$	$93_{\pm 6}$	$94_{\pm 7}$	$90_{\pm 7}$	$93_{\pm 4}$	$94_{\pm 6}$
PIW (↓)	$74_{\pm 5}$	$176_{\pm 18}$	$\underline{70_{\pm 6}}$	$127_{\pm 70}$	$96_{\pm 19}$	$77_{\pm 12}$	$110_{\pm 7}$	$112_{\pm 5}$

The best model is underlined. ML: Machine learning; CP: conformal prediction; GPR: Gaussian process regression; RBF: LM: linear mean; NN: neural network; RF: random forest; LGBM: light gradient boosting machine; MAE: mean absolute error; PIW: prediction interval width.

Table 7. Results for constraint C3 (martensite start temperature) using ML models with 10-fold cross-validation and distance-weighted cross-CP

Metric	Linear regression	Polynomial regression	GPR (RBF + LM)	GPR (Polynomial)	NN (Monotone)	GPR (RBF)	RF	LGBM
R^2 (↑)	$0.7_{\pm 0.1}$	$0.21_{\pm 0.07}$	$\underline{0.90_{\pm 0.02}}$	$0.88_{\pm 0.03}$	$0.09_{\pm 0.07}$	$0.90_{\pm 0.02}$	$0.91_{\pm 0.01}$	$0.91_{\pm 0.02}$
MAE (↓)	$29_{\pm 2}$	$63_{\pm 3}$	$\underline{19_{\pm 2}}$	$20_{\pm 2}$	$65.2_{\pm 6.1}$	$19_{\pm 2}$	$18_{\pm 1}$	$18_{\pm 1}$
cov (90%)	$90_{\pm 2}$	$90_{\pm 3}$	$\underline{92_{\pm 3}}$	$90_{\pm 3}$	$90.2_{\pm 3.6}$	$91_{\pm 2}$	$90_{\pm 3}$	$91_{\pm 2}$
PIW (↓)	$116_{\pm 5}$	$252_{\pm 6}$	$\underline{93_{\pm 7}}$	$97_{\pm 10}$	$258.2_{\pm 6.3}$	$90_{\pm 2}$	$83_{\pm 3}$	$85_{\pm 2}$

The best model is underlined. ML: Machine learning; CP: conformal prediction; GPR: Gaussian process regression; RBF: LM: linear mean; NN: neural network; RF: random forest; LGBM: light gradient boosting machine; MAE: mean absolute error; PIW: prediction interval width.

Table 8. Results for constraint C5 (martensite start temperature of retained austenite) using ML models with 10-fold cross-validation and distance-weighted cross-CP

Metric	Linear Regression	Polynomial Regression	GPR (RBF + LM)	GPR (Polynomial)	NN (Monotone)	GPR (RBF)	RF	LGBM
R^2 (↑)	$0.75_{\pm 0.07}$	$0.22_{\pm 0.03}$	$\underline{0.88_{\pm 0.03}}$	$0.87_{\pm 0.03}$	$0.05_{\pm 0.07}$	$0.89_{\pm 0.03}$	$0.90_{\pm 0.03}$	$0.90_{\pm 0.01}$
MAE (↓)	$30_{\pm 2}$	$63_{\pm 2}$	$\underline{20_{\pm 2}}$	$21_{\pm 2}$	$68_{\pm 3}$	$20_{\pm 2}$	$19_{\pm 2}$	$19_{\pm 1}$
cov (90%)	$91_{\pm 2}$	$90_{\pm 3}$	$\underline{92_{\pm 2}}$	$90_{\pm 4}$	$91_{\pm 3}$	$91_{\pm 2}$	$90_{\pm 4}$	$91_{\pm 1}$
PIW (↓)	$119_{\pm 3}$	$255_{\pm 4}$	$\underline{96_{\pm 7}}$	$103_{\pm 20}$	$269_{\pm 4}$	$94_{\pm 6}$	$88_{\pm 4}$	$88_{\pm 2}$

The best model is underlined. ML: Machine learning; CP: conformal prediction; GPR: Gaussian process regression; RBF: LM: linear mean; NN: neural network; RF: random forest; LGBM: light gradient boosting machine; MAE: mean absolute error; PIW: prediction interval width.

close to the desired 90%, validating the reliability of CP. GPR with an RBF kernel and LM shows the best performance in terms of the MAE and the smallest PIW, for all three constraints. It combines the flexibility of local models (such as GPR with RBF, RF, and LGBM), which on average outperform global models, with the ability of global models to effectively capture broader trends. We selected the GPR with an RBF kernel and LM because of the lower MAE and PIW for the final evaluation for these cases. The similarity in model results for the two martensite start temperature problems is expected because they share a significant fraction of their training data.

A key challenge in modeling the boundary condition C4, i.e., the logarithmic bainite transformation time $[\log_{10}(t_{90\%})]$, is the scarcity of data for transformation times exceeding the 3-hour constraint. This results in limited coverage for long-duration experiments. Additionally, transformation times span several orders of magnitude, necessitating the use of log-transformed targets to stabilize variance and improve model performance. The underlying behavior is monotonic in the chemical elements and has a C-shape in temperature. The results of the ML models are shown in Table 9, and the best-performing model is visualized in Figure 6E. Notably, data points outside the prediction interval are more frequent in regions of high or low transformation times.

Table 9. Results for constraint C4 [logarithmic bainite transformation time $\log_{10}(t_{90\%})$] using ML models with 10-fold cross-validation and distance-weighted cross-CP

Metric	<u>Linear regression+</u>	Polynomial regression	GPR (RBF + LM)	GPR (Polynomial)	NN (Monotone)	GPR (RBF)	RF	LGBM
R^2 (↑)	<u>$0.7_{\pm0.2}$</u>	$-1_{\pm3}$	$0.5_{\pm0.7}$	$-1_{\pm3}$	$0.3_{\pm0.5}$	$0.7_{\pm0.1}$	$0.6_{\pm0.2}$	$0.6_{\pm0.1}$
MAE (↓)	<u>$0.3_{\pm0.1}$</u>	$0.6_{\pm0.2}$	$0.3_{\pm0.2}$	$0.4_{\pm0.3}$	$0.4_{\pm0.1}$	$0.27_{\pm0.06}$	$0.4_{\pm0.2}$	$0.33_{\pm0.09}$
cov (90%)	<u>$91_{\pm11}$</u>	$94_{\pm7}$	$90_{\pm15}$	$90_{\pm12}$	$93_{\pm6}$	$95_{\pm8}$	$89_{\pm17}$	$94_{\pm6}$
PIW (↓)	<u>$1.4_{\pm0.1}$</u>	$2.6_{\pm0.4}$	$1.7_{\pm0.7}$	$2_{\pm1}$	$2.0_{\pm0.4}$	$1.4_{\pm0.2}$	$1.7_{\pm0.1}$	$1.7_{\pm0.2}$

The best model is underlined. ML: Machine learning; CP: conformal prediction; GPR: Gaussian process regression; RBF: LM: linear mean; NN: neural network; RF: random forest; LGBM: light gradient boosting machine; MAE: mean absolute error; PIW: prediction interval width.

Table 10. Comparison of test results for constraint C6 [logarithmic critical cooling rate of ferrite $\log_{10}(\dot{T}_{\mathrm{crit}})$] using ML models with 10-fold cross-validation and distance-weighted cross-CP

Metric	Linear regression	Polynomial regression	GPR (RBF)	GPR (Polynomial)	NN	<u>RF</u>	XGBoost	LGBM
R^2 (↑)	$0.2_{\pm0.3}$	$-0.5_{\pm0.9}$	$0.6_{\pm0.2}$	$-0_{\pm1}$	$0.1_{\pm0.8}$	<u>$0.7_{\pm0.2}$</u>	$0.6_{\pm0.2}$	$0.6_{\pm0.3}$
MAE (↓)	$0.7_{\pm0.1}$	$0.9_{\pm0.2}$	$0.5_{\pm0.1}$	$0.7_{\pm0.3}$	$0.6_{\pm0.2}$	<u>$0.43_{\pm0.09}$</u>	$0.44_{\pm0.08}$	$0.44_{\pm0.11}$
cov (90%)	$93_{\pm5}$	$91_{\pm7}$	$91_{\pm8}$	$92_{\pm7}$	$92_{\pm5}$	<u>$91_{\pm7}$</u>	$92_{\pm5}$	$92_{\pm7}$
PIW (↓)	$3.3_{\pm0.1}$	$3.6_{\pm0.2}$	$2.3_{\pm0.2}$	$3.1_{\pm0.5}$	$2.8_{\pm0.2}$	<u>$2.2_{\pm0.2}$</u>	$2.5_{\pm0.2}$	$2.2_{\pm0.2}$

The best model is underlined. ML: Machine learning; CP: conformal prediction; GPR: Gaussian process regression; RBF: LM: linear mean; NN: neural network; RF: random forest; LGBM: light gradient boosting machine; MAE: mean absolute error; PIW: predic-tion interval width.

While GPR with an RBF kernel achieves the lowest MAE for C4, it struggles with extrapolation, especially when constrained by the limited training data. Assuming that transformation times are approximately monotonic with respect to alloy composition, we can improve linear regression with quadratic temperature features $[T^2,\ \log_{10}(T)^2]$. Despite achieving a slightly lower R^2, it provides interpretable predictions with stable linear extrapolation and monotonicity, making it the preferred model for deployment in extrapolative regions. Thus, it is selected for the final evaluation. The coverage remained close to the desired 90%. However, the variability of the coverage is higher than in previous tasks, with standard deviations up to 11%, and the width of the prediction interval is relatively large, spanning at least 1.4 orders of magnitude. This can be explained by a suboptimal model performance. As a result, some folds may overestimate or underestimate the uncertainty, especially in regions where data is sparse or the target values span a wide range. Despite this variability, distance-aware CP still demonstrates its robustness by achieving reasonable coverage.

The critical cooling rate of ferrite, i.e., C6, also spans several orders of magnitude. For this reason, similar to the bainite transformation time, predicting $\log_{10}(\dot{T}_{\mathrm{crit}})$ provides more stability. The predictive performance of the ML regression models is listed in Table 10, and the result of the best model is shown in Figure 6F.

The results for C6 reveal notable variability in the models' performance. Particularly noteworthy are the performances of the GPR with a polynomial kernel and the NN. Both models exhibit a high MAE, indicating poor predictions for certain data points, despite achieving high coverage and a low PIW. This highlights their failure to accurately predict a few critical samples. Among the evaluated methods, local models such as RFs, XGBoost and GPR achieve the lowest MAE scores of 0.43 ± 0.09, 0.44 ± 0.08, and 0.44 ± 0.1, respectively. This suggests that these models are better suited for capturing the nonlinear relationships in the dataset compared to linear or polynomial regression. The coverage of the CP intervals remains stable across all models, averaging close to the desired 90%, with slight variability due to the relatively small dataset size. Notably, RFs and LGBM perform very similarly; however, because of the higher R^2 value, the RFs are selected.

To get insight into which features are responsible for the model prediction, SHapley Additive exPlanations

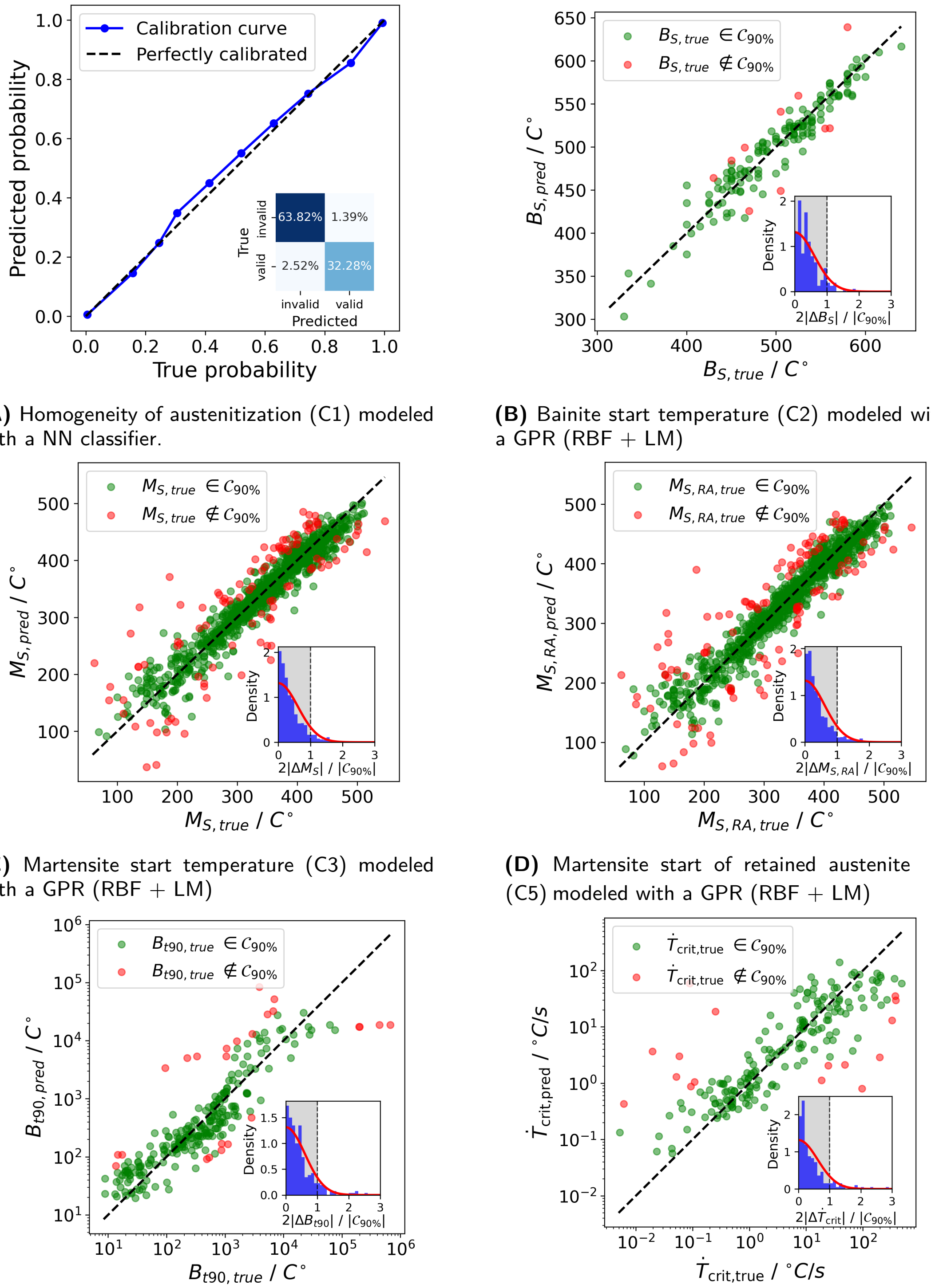

(A) Homogeneity of austenitization (C1) modeled with a NN classifier.

(B) Bainite start temperature (C2) modeled with a GPR (RBF + LM)

(C) Martensite start temperature (C3) modeled with a GPR (RBF + LM)

(D) Martensite start of retained austenite (C5) modeled with a GPR (RBF + LM)

(E) Bainite transformation time (C4) modeled with a linear regression

(F) Critical cooling rate of ferrite (C6) modeled with a RF

Figure 6. Calibration curve and confusion matrix for the classification task (C1). Predicted test values versus true values for the constraints treated as regression problems (C2-C6).

(SHAP) analysis is employed [84]. The resulting SHAP values quantify the marginal contribution of each feature, where the sign of the SHAP value indicates whether the feature increases or decreases the prediction, and the magnitude reflects the strength of its influence.

The SHAP values for the prediction models are shown in Figure 7. For condition C1 [Figure 7A], high concentrations of aluminum (Al), silicon (Si), and vanadium (V) increase the likelihood of successful austenitization. However, the effect of carbon (C) remains ambiguous. This is attributed to its dual role: while carbon stabilizes austenite and lowers the austenitization temperature into the valid range, it also promotes carbide formation.

For the bainite start temperature (C2) [Figure 7B], and the martensite start temperatures (C3 and C5) [Figure 7C and D], the SHAP values exhibit a monotonic and approximately linear dependence on concentration, reflecting the LM function of the employed GPR model. Notably, in Figure 7B, carbon does not yield the highest SHAP value despite its substantial influence per wt.%. This discrepancy arises from feature distribution effects within the dataset. A similar pattern is observed for Al and V, which appear less influential due to their limited high-concentration data points.

For bainite transformation time (C4) [Figure 7E], SHAP values highlight manganese (Mn), C, and nickel (Ni) as the dominant factors contributing to prolonged transformation times, while also revealing the nonlinear influence of temperature. Finally, for the critical cooling rate (C6), the SHAP values in Figure 7F indicate complex and inconclusive trends for several elements, particularly for molybdenum (Mo).

Design space

To evaluate the reduction of the design space, the best-performing models for each constraint were applied to 10^6 evaluation points sampled uniformly for the dimensions C, Si, Mn, Cr, Al, V, Mo, T_{iso} and $\log_{10}(\dot{T}_{\mathrm{crit}})$ within the boundaries defined in Table 2. In modeling the process-dependent constraints C4 and C5, we implicitly assumed that the isothermal holding temperature complies with constraints C2 and C3. This assumption is grounded in the observation that predicting bainite transformation times above the bainite start temperature is inherently illogical. Furthermore, the formation of martensite before bainite significantly accelerates the bainite transformation process[85]. The reduction of the design space was evaluated using three tolerances: low, mid, and high. The mid-tolerance evaluation utilized the mean predictions from the models, while the low tolerance employs the bound of the CP interval which results in a smaller design space, thereby imposing a more stringent constraint. In contrast, the high tolerance evaluation applies the upper bound of the interval, effectively relaxing the constraint. A visualization for the example of C2 (B_{S}) and C3 (M_{S}) is given in Figure 8. For low tolerance, the upper confidence interval for M_{S} and the lower of B_{S} is taken, mid-tolerance is evaluated with the mean predictions and high tolerance is evaluated with the lower confidence intervals for M_{S} and the upper for B_{S}.

The results of these evaluations for both heat treatments are summarized in Figure 9. A significant difference is observed in the percentage of predicted CFB points between the isothermal holding and continuous cooling processes. However, this discrepancy does not reflect the full reality, as the constraint C7, shown in Figure 1, was not incorporated in this study due to missing data. This results in an overestimation of design space. Solving this issue will be part of future work, either by building a data-driven literature model or by direct prediction of bainite transformation kinetics. Furthermore, the increase in space from a higher tolerance level is much larger in the continuously cooled case, which can be explained by the higher uncertainty of constraint C6. At a high tolerance, the C6 constraint does not exclude any test points.

For further analysis of the constraints, we focus on the isothermal process and select the high tolerance criterion. This approach uses the calibrated uncertainty intervals to avoid prematurely excluding viable design regions. Even with a high tolerance, the design space is only 20% of the search space, which corresponds to an 80% reduction. The final relationship between each input dimension and the acceptance percentage for the different constraints is shown in Figure 10.

The acceptance percentage shown in Figure 10 is the probability that a point in the search space is CFB given

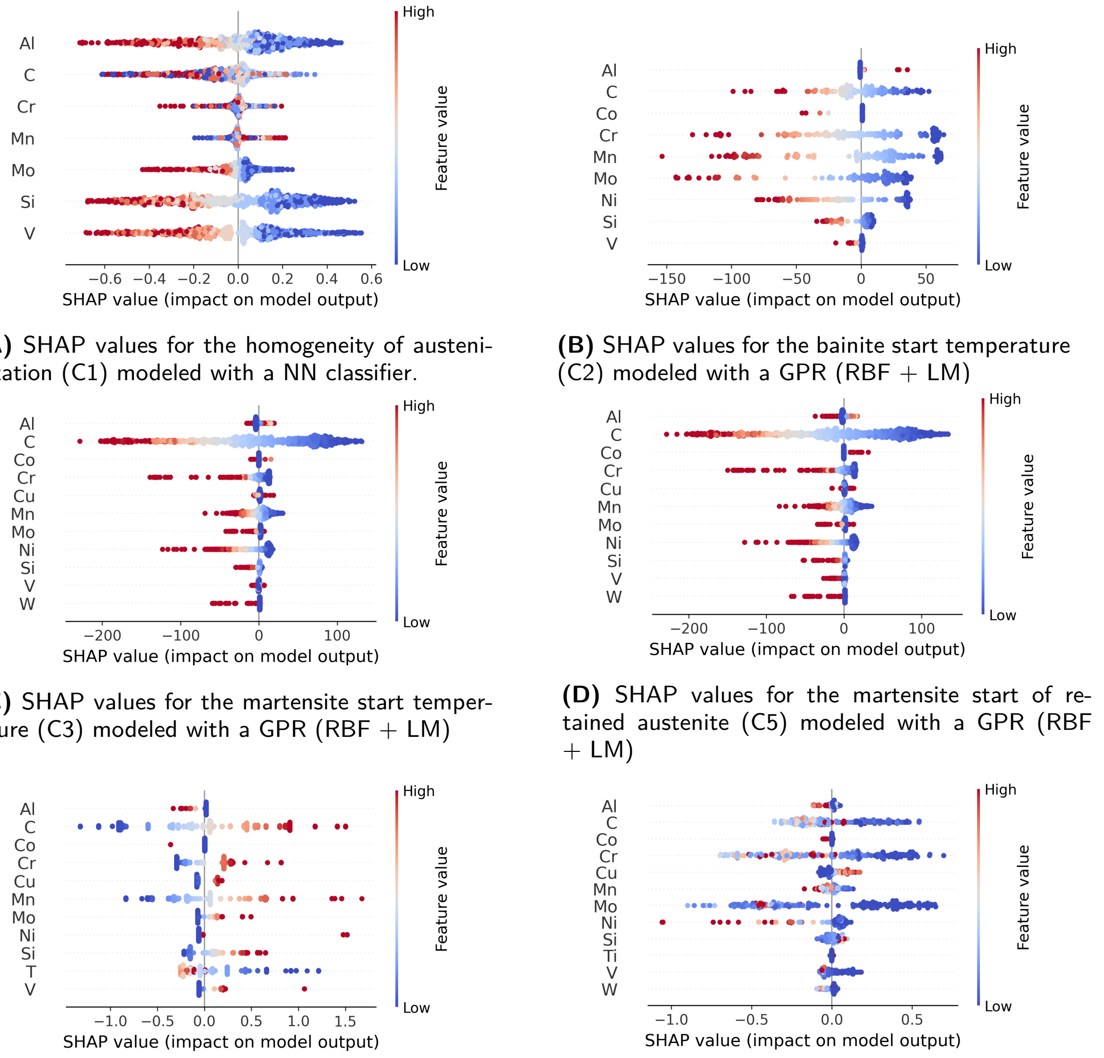

(A) SHAP values for the homogeneity of austenitization (C1) modeled with a NN classifier.

(B) SHAP values for the bainite start temperature (C2) modeled with a GPR (RBF + LM)

(C) SHAP values for the martensite start temperature (C3) modeled with a GPR (RBF + LM)

(D) SHAP values for the martensite start of retained austenite (C5) modeled with a GPR (RBF + LM)

(E) SHAP values for the bainite transformation time (C4) modeled with a linear regression

(F) SHAP values for the critical cooling rate of ferrite (C6) modeled with a RF

Figure 7. SHAP value analysis of models C1 to C6. Subplots (A) to (F) correspond to models C1 to C6, respectively, illustrating the contribution of each feature to the model predictions. SHAP: SHapley Additive exPlanations.

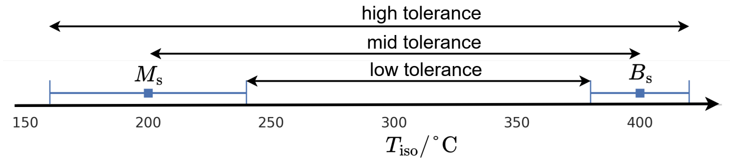

Figure 8. Tolerance levels.

that the value of one (in the case of Figure 10) or two (in the case of Figure 11) dimensions in the search space. For the remaining dimensions, values are sampled randomly from uniform distributions. Importantly, this percentage does not indicate the probability that a point is accepted during the process. To derive the overall

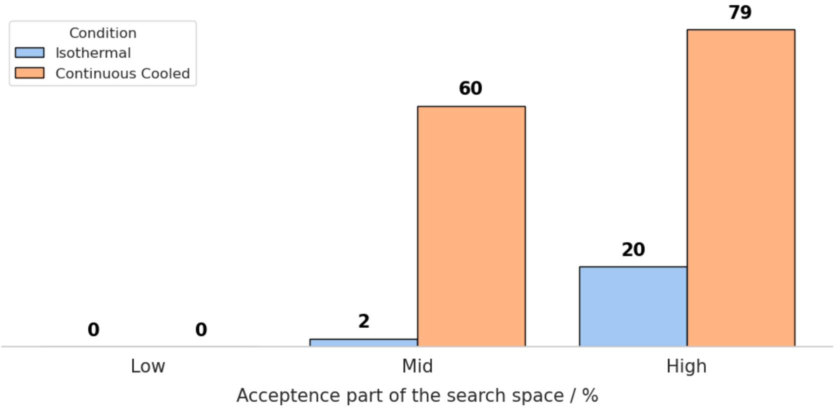

Figure 9. Design space reduction for the different heat treatments; see text for description for tolerance.

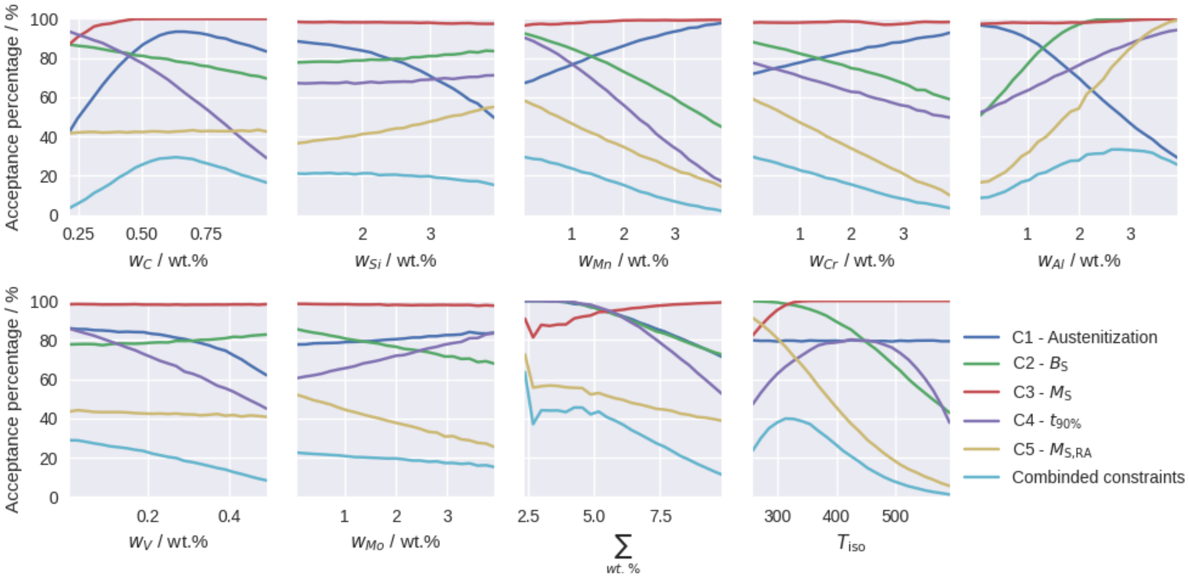

Figure 10. Acceptance percentage along design space dimensions.

acceptance rate of 20% as shown in Figure 9, the points must be aggregated, accounting for the occurrence rate.

A horizontal line in the acceptance percentage in Figure 10 for a single dimension indicates no dependency. For instance, C1 (austenitization) is completely independent of T_{iso}. For C1, carbon exhibits a maximum acceptance percentage of around 0.7 wt.%, which reflects its dual role: stabilizing both carbides and austenite. Further interpretation is challenging due to the complex interplay between the stabilization of austenite, the destabilization of ferrite, and the destabilization of carbides under the austenitization condition. The behavior of the bainite start temperature (C2) aligns with expectations: acceptance percentages decrease with increasing alloying content, isothermal holding temperature, and the concentrations of all elements except aluminum. The martensite start temperature of the initial alloy (C3) does not act as a filtering constraint under low tolerance. For the transformation time (C4), overall alloying content has the most significant influence, as expected. Dependencies on molybdenum and the transformation speed acceleration effect of aluminum are consistent with previous findings[86,87]. The constraint related to the martensite start temperature of the retained austenite (C5) reflects a complex interplay between the carbon solubility of alloying elements and the

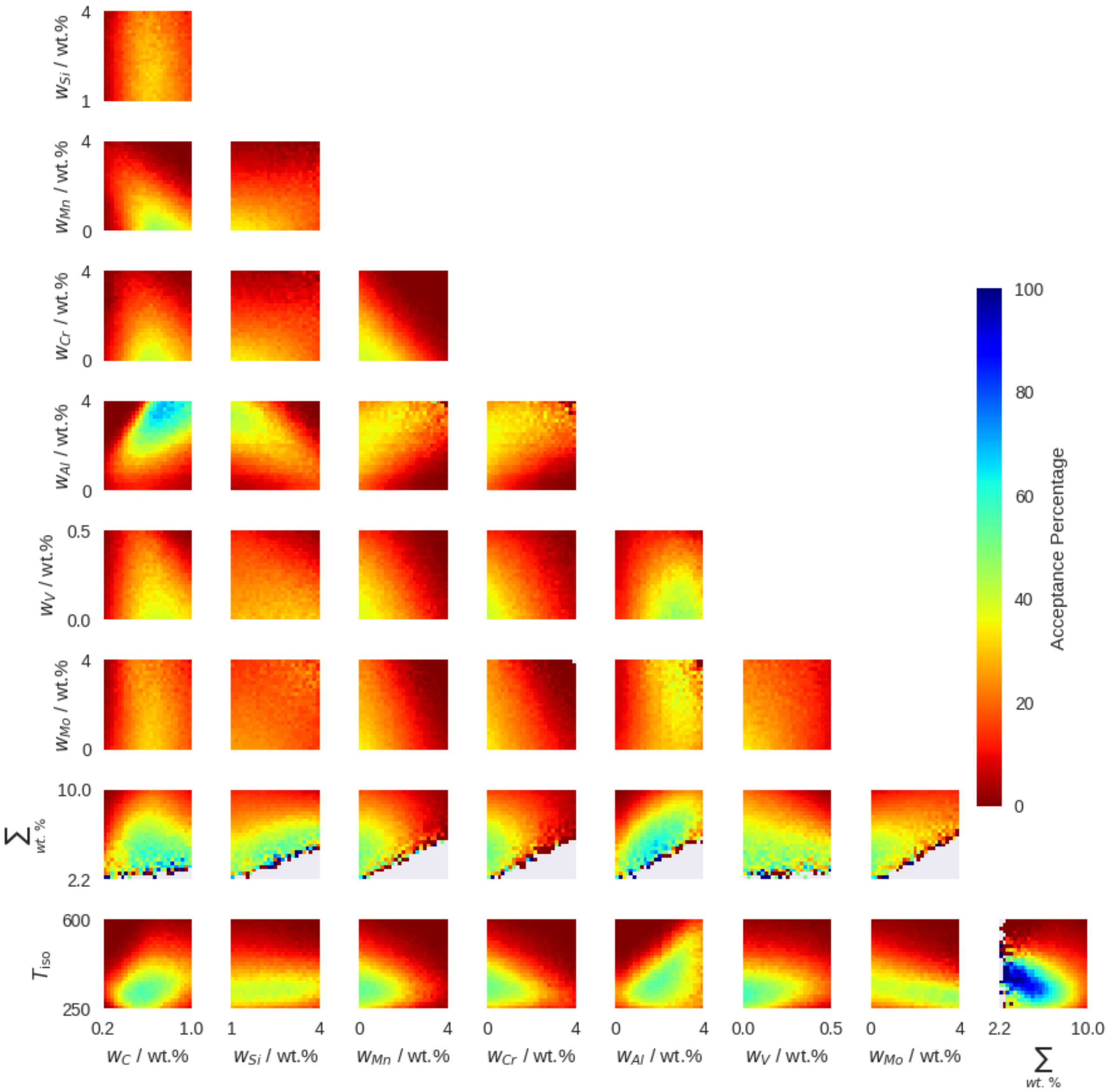

Figure 11. Acceptance percentage for two element interaction.

chemical dependency of martensite start. Positive correlations for silicon and aluminum are attributed to their effects on carbon solubility in retained austenite: silicon decreases solubility only slightly, while aluminum even increases it[31]. The acceptance percentages of the combined constraints exhibit maxima for carbon and isothermal holding temperature, negative correlations with manganese, chromium, and molybdenum, and positive correlations with aluminum. These rates are also strongly influenced by the total alloying element concentration.

The two-element interaction for the rejection rate is shown in Figure 11. Regardless of the specific alloying elements, low total alloy element concentrations $\sum_{\mathrm{wt.\%}}$ exhibit the highest acceptance percentages by a significant margin, visualized by the dark blue areas. The gray areas in the diagram denote regions without data points, as the total alloy element concentration cannot be lower than the concentration of the other element in the binary diagram. The dark red areas signify areas of low acceptance percentages. They are often positioned in a corner, which shows an interaction of the dimensions. For example, high molybdenum concentrations are mutually exclusive with high concentrations of chromium. No significant interaction is indicated if a diagram looks the same along one dimension. This would be the case for molybdenum and vanadium.

CONCLUSION

In this work, we present a novel approach to model design spaces for optimization problems with categorical constraints on the example of CFB steels.

- The classification problem (CFB/non-CFB) is split into physically feasible and consistent parts, constraints C1 to C6.
- For these constraints, we produce 21 more experimental data points.
- ML models are applied to predict the constraints, and we address several challenges, including limited data, class imbalances, monotonicity constraints, and robust uncertainty estimation.
- To minimize the exclusion of potentially valuable candidates due to incorrect predictions, we introduced distance-aware CP to produce calibrated uncertainty intervals for both probabilistic and deterministic models. This allows for adjusting confidence to a desired level for classification; in this work, we picked the upper 90th percentile.
- This results in a classifier for CFB. Using mean predictions for constraints reduced the design space to 2% of the total samples. However, incorporating CP-based uncertainty estimates expanded the valid design space to 20%, preserving potentially useful candidates for further exploration while allowing a higher sample efficiency in future design of CFB steel.

In the future, this framework will support the Bayesian optimization of CFB steel. Reliable uncertainty estimation will help to balance the trade-off between reducing the design space and maintaining sufficient exploration.

DECLARATIONS

Acknowledgments

We would like to thank Philipp Retzl and MatCalc Engineering GmbH for their help in setting up high throughput calculations in MatCalc.

Authors' contributions

Made substantial contributions to conception and design of the study, and performed data analysis, interpretation and writing: Schuscha, B.; Steger, S.
Provided supervision, administrative and technical support, writing assistance and proofreading: Pernkopf, F.; Brandl, D.; Scheiber, D.; Romaner, L.

Availability of data and materials

The datasets and codes used in the present work are available at https://github.com/BerndSchuscha/bainite_boundaries.

Financial support and sponsorship

The authors gratefully acknowledge the financial support under the scope of the COMET program within the K2 Center "Integrated Computational Material, Process and Product Engineering (IC-MPPE)" (Project No. 886385). This program is supported by the Austrian Federal Ministries for Climate Action, Environment, Energy, Mobility, Innovation and Technology (BMK) and for Digital and Economic Affairs (BMDW), represented by the Austrian Research Promotion Agency (FFG), and the federal states of Styria, Upper Austria and Tyrol.

Conflicts of interest

All authors declared that there are no conflicts of interest.

Ethical approval and consent to participate

Not applicable.

Consent for publication

Not applicable.

Copyright

REFERENCES

1. Shahriari, B.; Swersky, K.; Wang, Z.; Adams, R. P.; de Freitas, N. Taking the human out of the loop: a review of Bayesian optimization. *Proc. IEEE.* **2016**, *104*, 148–75. DOI
2. Lookman, T.; Balachandran, P.; Xue, D.; Yuan, R. Active learning in materials science with emphasis on adaptive sampling using uncertainties for targeted design. *npj. Comput. Mater.* **2019**, *5*, 21. DOI
3. Balachandran, P. V.; Xue, D.; Theiler, J.; Hogden, J.; Lookman, T. Adaptive strategies for materials design using uncertainties. *Sci. Rep.* **2016**, *6*, 19660. DOI
4. Shi, B.; Zhou, Y.; Fang, D.; et al. Estimating the performance of a material in its service space via Bayesian active learning: a case study of the damping capacity of Mg alloys. *J. Mater. Inf.* **2022**, *2*, 8. DOI
5. Giles, S. A.; Sengupta, D.; Broderick, S. R.; Rajan, K. Machine-learning-based intelligent framework for discovering refractory high-entropy alloys with improved high-temperature yield strength. *npj. Comput. Mater.* **2022**, *8*, 235. DOI
6. Khatamsaz, D.; Vela, B.; Singh, P.; Johnson, D.; Allaire, D.; Arróyave R. Bayesian optimization with active learning of design constraints using an entropy-based approach. *npj. Comput. Mater.* **2023**, *9*, 49. DOI
7. Moitzi, F.; Romaner, L.; Ruban, A. V.; Hodapp, M.; Peil, O. E. Ab initio framework for deciphering trade-off relationships in multi-component alloys. *npj. Comput. Mater.* **2024**, *10*, 152. DOI
8. Bouquerel, J.; Verbeken, K.; De Cooman, B. C. Microstructure-based model for the static mechanical behaviour of multiphase steels. *Acta. Mater.* **2006**, *54*, 1443–56. DOI
9. Bramfitt, B. L. Structure/property relationships in irons and steels. In: Metals Handbook Desk Edition. ASM International; 1998. pp. 153-73. DOI
10. Bhadeshia, H. K. D. H.; Honeycombe, R. W. K. Steels: microstructure and properties. 4th edition. Butterworth-Heinemann; 2017. https://shop.elsevier.com/books/steels-microstructure-and-properties/bhadeshia/978-0-08-100270-4. (accessed 2025-03-10)
11. Alibeyki, M.; Mirzadeh, H.; Najafi, M.; Kalhor, A. Modification of rule of mixtures for estimation of the mechanical properties of dual phase steels. *J. Mater. Eng. Perform.* **2017**, *26*, 2683–8. DOI
12. Prawoto, Y.; Djuansjah, J. R. P.; Shaffiar, N. B. Re-visiting the 'rule of mixture' used in materials with multiple constituting phases: a technical note on morphological considerations in austenite case study. *Comput. Mater. Sci.* **2012**, *65*, 528–35. DOI
13. Bouaziz, O.; Buessler, P. Mechanical behaviour of multiphase materials: an intermediate mixture law without fitting parameter. *Rev. Met. Paris.* **2002**, *99*, 71-7. DOI
14. Bhadeshia, H. K. D. H. Bainite in steels - Theory and practice. 3rd edition. CRC Press; 2015. DOI
15. Low, A. K. Y.; Vissol-Gaudin, E.; Lim, Y. F.; Hippalgaonkar, K. Mapping pareto fronts for efficient multi-objective materials discovery. *J. Mater. Inform.* **2023**, *3*, 11. DOI
16. Khatamsaz, D.; Vela, B.; Singh, P.; Johnson, D. D.; Allaire, D.; Arróyave, R. Multi-objective materials bayesian optimization with active learning of design constraints: design of ductile refractory multi-principal-element alloys. *Acta. Mater.* **2022**, *236*, 118133. DOI
17. Quionero-Candela, J.; Sugiyama, M.; Schwaighofer, A.; Lawrence, N. D. Dataset shift in machine learning. The MIT Press; 2009. https://mitpress.mit.edu/9780262545877/dataset-shift-in-machine-learning/. (accessed 2025-03-10)
18. Malinin, A.; Gales, M. Predictive uncertainty estimation via prior networks. *arXiv* **2018**, arXiv:1802.10501. Available online: https://doi.org/10.48550/arXiv.1802.10501. (accessed on 10 Mar 2025)
19. Cuomo, S.; Di Cola, V. S.; Giampaolo, F.; Rozza, G.; Raissi, M.; Piccialli, F. Scientific machine learning through physics-informed neural networks: where we are and what's next. *J. Sci. Comput.* **2022**, *92*, 88. DOI
20. Papadopoulos, H. Guaranteed coverage prediction intervals with Gaussian process regression. *IEEE. Trans. Pattern. Anal. Mach. Intell.* **2024**, *46*, 9072-83. DOI
21. Vovk, V.; Gammerman, A.; Shafer, G. Algorithmic learning in a random world. 1st edition. Springer; 2005. DOI
22. Angelopoulos AN, Bates S. A gentle introduction to conformal prediction and distribution-free uncertainty quantification. *arXiv* **2021**, arXiv:2107.07511. Available online: https://doi.org/10.48550/arXiv.2107.07511. (accessed on 10 Mar 2025)
23. Tibshirani, R. J.; Foygel Barber, R.; Candes, E.; Ramdas, A. Conformal prediction under covariate shift. *arXiv* **2019**, arXiv:1904.06019. Available online: https://doi.org/10.48550/arXiv.1904.06019. (accessed on 10 Mar 2025)

24. Caballero, F. G. 12 - Carbide-free bainite in steels. In: Pereloma E, Edmonds DV, editors. Phase Transformations in steels. vol. 1 of Woodhead Publishing Series in Metals and Surface Engineering. Woodhead Publishing; 2012. pp. 436–67. DOI
25. Zhu, K.; Mager, C.; Huang, M. Effect of substitution of Si by Al on the microstructure and mechanical properties of bainitic transformation-induced plasticity steels. *J. Mater. Sci. Technol.* **2017**, *33*, 1475–86. DOI
26. Sugimoto, K. Effects of partial replacement of Si by Al on cold formability in two groups of low-carbon third-generation advanced high-strength steel sheet: a review. *Metals* **2022**,*12*, 2069. DOI
27. Lukas, H.; Fries, S. G.; Sundman, B. Computational thermodynamics: the calphad method. Cambridge University Press; 2007. DOI
28. Kozeschnik, E. Mean-field microstructure kinetics modeling. In: Caballero FG, editor. Encyclopedia of Materials: Metals and Alloys. Oxford: Elsevier; 2022. pp. 521–6. DOI
29. van Bohemen, S. M. C. Bainite and martensite start temperature calculated with exponential carbon dependence. *Mater. Sci. Technol.* **2012**, *28*, 487–95. DOI
30. Leach, L.; Kolmskog, P.; Höglund, L.; Hillert, M.; Borgenstam, A. Use of Fe-C information as reference for alloying effects on B_S. *Metall. Mater. Trans. A.* **2019**, *50*, 4531-40. DOI
31. Schuscha, B.; Brandl, D.; Romaner, L.; et al. Predictive modeling of the Bainite start temperature using Bayesian inference. *Acta. Mater.* **2024**. DOI
32. Leach, L.; Kolmskog, P.; Höglund, L.; Hillert, M.; Borgenstam, A. Critical driving forces for formation of Bainite. *Metall. Mater. Trans. A* **2018**, *49*, 4509-20. DOI
33. Lu, Q.; Liu, S.; Li, W.; Jin, X. Combination of thermodynamic knowledge and multilayer feedforward neural networks for accurate prediction of MS temperature in steels. *Mater. Design* **2020**, *192*, 108696. DOI
34. Li, M. V.; Niebuhr, D. V.; Meekisho, L. L.; Atteridge, D. G. A computational model for the prediction of steel hardenability. *Metall. Mater. Trans. B* **1998**, *29*, 661–72. DOI
35. Martin, H.; Amoako-Yirenkyi, P.; Pohjonen, A.; Frempong, N. K.; Komi, J.; Somani, M. Statistical modeling for prediction of CCT diagrams of steels involving interaction of alloying elements. *Metall. Mater. Trans. B* **2020**, *52*, 223-35. DOI
36. Geng, X.; Wang, H.; Xue, W.; et al. Modeling of CCT diagrams for tool steels using different machine learning techniques. *Comput. Mater. Sci.* **2020**, *171*, 109235. DOI
37. Minamoto, S.; Tsukamoto, S.; Kasuya, T.; Watanabe, M.; Demura, M. Prediction of continuous cooling transformation diagram for weld heat affected zone by machine learning. *Sci. Technol. Adv. Mat.* **2022**, *2*, 402–15. DOI
38. Huang, X.; Wang, H.; Xue, W.; et al. A combined machine learning model for the prediction of time-temperature-transformation diagrams of high-alloy steels. *J. Alloys. Compd.* **2020**, *823*, 153694. DOI
39. Povoden-Karadeniz, E. MatCalc thermodynamic steel database, version 2.061, 2023. https://www.matcalc.at/images/stories/Download/Database/mc_fe_v2061.tdb. (accessed 2025-03-10)
40. Presoly, P.; Gerstl, B.; Bernhard, C.; et al. Primary carbide formation in tool steels: potential of selected laboratory methods and potential of partial premelting for the generation of thermodynamic data. *Steel. Res. Int.* **2022**, *94*, 2200503. DOI
41. Presoly, P.; Pierer, R.; Bernhard, C. Identification of defect prone peritectic steel grades by analyzing high-temperature phase transformations. *Metall. Mater. Trans. A* **2013**, *44*, 5377–88. DOI
42. Verein Deutscher Eisenhüttenleute Unterausschuss für Metallographie, Werkstoffanalytik und -simulation. Guidelines for preparation, execution and evaluation of dilatometric transformation tests on iron alloys. Verlag Stahleisen GmbH; 1998. https://books.google.com/books/about/Guidelines_for_preparation_execution_and.html?id=R6-d0AEACAAJ. (accessed 2025-03-10)
43. Williams, C. K. I.; Rasmussen, C. Gaussian processes for regression. In: *Advances in neural information processing systems*. MIT Press; 1995. https://proceedings.neurips.cc/paper/1995/hash/7cce53cf90577442771720a370c3c723-Abstract.html. (accessed 2025-03-10)
44. Rasmussen, C. E.; Williams, C. K. I. Gaussian processes for machine learning. MIT Press; 2005. DOI
45. Breiman, L. Random forests. *Mach. Learn.* **2001**, *45*, 5–32. DOI
46. Friedman, J.; Hastie, T.; Tibshirani, R. Additive logistic regression: a statistical view of boosting (with discussion and a rejoinder by the authors). *Ann. Statist.* **2000**, *28*, 337–407. DOI
47. Fiedler, C.; Scherer, C. W.; Trimpe, S. Practical and rigorous uncertainty bounds for Gaussian process regression. *AAAI Conf. Artif. Intell.* **2021**, *35*, 7439–47. DOI
48. Goodfellow, I.; Bengio, Y.; Courville, A. Deep Learning. MIT Press; 2016. https://www.deeplearningbook.org/. (accessed 2025-03-10)
49. Kitouni, O.; Nolte, N.; Williams, M. Expressive monotonic neural networks. *arXiv* **2023**, arXiv:2307.07512. Available online: https://doi.org/10.48550/arXiv.2307.07512. (accessed on 10 Mar 2025)
50. Boser, B. E.; Guyon, I. M.; Vapnik, V. N. A training algorithm for optimal margin classifiers. In: Proceedings of the fifth annual workshop on Computational learning theory. Association for Computing Machinery, 1992; pp. 144–52. DOI
51. D'Angelo, F.; Henning, C. On out-of-distribution detection with Bayesian neural networks. *arXiv* **2021**, arXiv:2110.06020. Available online: https://doi.org/10.48550/arXiv.2110.06020. (accessed on 10 Mar 2025)
52. Hüllermeier, E.; Waegeman, W. Aleatoric and epistemic uncertainty in machine learning: an introduction to concepts and methods. *Mach. Learn.* **2021**, *110*, 457–506. DOI
53. Gruber, C.; Schenk, P.; Schierholz, M.; Kreuter, F.; Kauermann, G. Sources of uncertainty in machine learning - a statisticians' view. *arXiv* **2023**, arXiv:2305.16703. Available online: https://doi.org/10.48550/arXiv.2305.16703. (accessed on 10 Mar 2025)
54. Tran, K.; Neiswanger, W.; Yoon, J.; Zhang, Q.; Xing, E.; Ulissi, Z. W. Methods for comparing uncertainty quantifications for material property predictions. *Mach. Learn. Sci. Technol.* **2020**, *1*, 025006. DOI
55. Lahlou, S.; Jain, M.; Nekoei, H.; et al. DEUP: direct epistemic uncertainty prediction. *arXiv* **2021**, arXiv:2102.08501. Available online:

https://doi.org/10.48550/arXiv.2102.08501. (accessed on 10 Mar 2025)

56. Shafer, G.; Vovk, V. A tutorial on conformal prediction. *arXiv* **2007**, arXiv:0706.3188. Available online: https://doi.org/10.48550/arXiv.0706.3188. (accessed on 10 Mar 2025)
57. Papadopoulos, H.; Proedrou, K.; Vovk, V.; Gammerman, A. Inductive confidence machines for regression. In: *Machine learning: ECML 2002: 13th European conference on machine learning*, Helsinki, Finland, August 19–23, 2002. Springer, 2002; pp. 345–56. DOI
58. Papadopoulos, H.; Vovk, V.; Gammerman, A. Regression conformal prediction with nearest neighbours. *J. Artif. Intell. Res.* **2011**, *40*, 815–40. DOI
59. Bishop, C. M. Pattern recognition and machine learning. Berlin, Heidelberg: Springer-Verlag; 2006. https://link.springer.com/book/9780387310732. (accessed 2025-03-10)
60. Panaretos, V. M.; Zemel, Y. Statistical aspects of Wasserstein distances. *Annu. Rev. Stat. Appl.* **2019**, *6*, 405–31. DOI
61. McLachlan, G. J. Mahalanobis distance. *Reson.* **1999**, *4*, 20–6. DOI
62. Luo, C.; Zhan, J.; Wang, L.; Yang, Q. Cosine normalization: using cosine similarity instead of dot product in neural networks. *arXiv* **2017**, arXiv:1702.05870. Available online: https://doi.org/10.48550/arXiv.1702.05870. (accessed on 10 Mar 2025)
63. Damon, J.; Mühl, F.; Dietrich, S.; Schulze, V. A comparative study of kinetic models regarding Bainitic transformation behavior in carburized case hardening steel 20MnCr5. *Metall. Mater. Trans. A* **2018**, *50*, 104-17. DOI
64. Kumnorkaew, T.; Lian, J.; Uthaisangsuk, V.; Bleck, W. Kinetic model of isothermal Bainitic transformation of low carbon steels under ausforming conditions. *Alloys* **2022**, *1*, 93–115. DOI
65. Lin, S.; Borgenstam, A.; Stark, A.; Hedström P. Effect of Si on bainitic transformation kinetics in steels explained by carbon partitioning, carbide formation, dislocation densities, and thermodynamic conditions. *Mater. Charact.* **2022**, *185*, 111774. DOI
66. Luzginova, N. V.; Zhao, L.; Wauthier, A.; Sietsma, J. The kinetics of the isothermal Bainite formation in 1 In: *Microalloying for New Steel Processes and Applications. vol. 500 of Materials Science Forum*. Trans Tech Publications Ltd; 2005. pp. 419–28. DOI
67. Morawiec, M.; Ruiz-Jimenez, V.; Garcia-Mateo, C.; Grajcar, A. Thermodynamic analysis and isothermal bainitic transformation kinetics in lean medium-Mn steels. *J. Therm. Anal. Calorim.* **2020**, *142*, 1709-19. DOI
68. Pei, W.; Liu, W.; Zhang, Y.; Qie, R.; Zhao, A. Study on kinetics of transformation in medium carbon steel Bainite at different isothermal temperatures. *Materials* **2021**, *14*, 2721. DOI
69. Quidort, D.; Bréchet, Y. The role of carbon on the kinetics of bainite transformation in steels. *Scr. Mater.* **2002**, *47*, 151–6. DOI
70. Quidort, D.; Brechet, Y. J. M. A model of isothermal and non isothermal transformation kinetics of bainite in 0.5 *ISIJ. Int.* **2002**, *42*, 1010–7. DOI
71. Babasafari, Z.; Pan, A. V.; Pahlevani, F.; Moon, S. C.; Du Toit, M.; Dippenaar, R. Kinetics of bainite transformation in multiphase high carbon low-silicon steel with and without pre-existing martensite. *Metals* **2022**, *12*, 1969. DOI
72. Ravi, A.; Kumar, A.; Herbig, M.; Sietsma, J.; Santofimia, M. J. Impact of austenite grain boundaries and ferrite nucleation on bainite formation in steels. *Acta. Mater.* **2020**, *188*, 424-34. DOI
73. Singh, S. B.; Bhadeshia, H. K. D. H. Quantitative evidence for mechanical stabilization of bainite. *Mater. Sci. Technol.* **1996**, *12*, 610–2. DOI
74. Sourmail, T.; Smanio, V. Influence of cobalt on Bainite formation kinetics in 1 Pct C steel. *Metall. Mater. Trans. A* **2013**, *44*, 1975-8. DOI
75. van Bohemen, S. M. C.; Sietsma, J. Modeling of isothermal bainite formation based on the nucleation kinetics. *Int. J. Mater. Res.* **2008**, *99*, 739–47. DOI
76. van Bohemen, S. M. C.; Sietsma, J. The kinetics of bainite and martensite formation in steels during cooling. *Mater. Sci. Eng. A.* **2010**, *527*, 6672–6. DOI
77. van Bohemen, S. M. C.; Hanlon, D. N. A physically based approach to model the incomplete bainitic transformation in high-Si steels. *Int. J. Mater. Res.* **2012**, *103*, 987–91. DOI
78. van Bohemen, S. M. C. Bainite growth retardation due to mechanical stabilisation of austenite. *Materialia* **2019**, *7*, 100384. DOI
79. Gao, B.; Tan, Z.; Tian, Y.; et al. Accelerated isothermal phase transformation and enhanced mechanical properties of railway wheel steel: the significant role of pre-existing Bainite. *Steel. Res. Int.* **2022**, *93*, 2100494. DOI
80. Kang, J.; Zhang, F. C.; Yang, X. W.; Lv, B.; Wu, K. M. Effect of tempering on the microstructure and mechanical properties of a medium carbon bainitic steel. *Mater. Sci. Eng. A* **2017**, *686*, 150-9. DOI
81. Sage, A. M. Atlas of continuous cooling transformation diagrams for vanadium steels. Vanitec Publication; 1985. https://vanitec.org/technical-library/paper/atlas-of-continuous-cooling-transformation-diagrams-for-vanadium-steels. (accessed 2025-03-10)
82. Vander Voort, G. F. Atlas of time-temperature diagrams for irons and steels. ASM International; 1991. https://app.knovel.com/kn/resources/kpATTDIS05/toc. (accessed 2025-03-10)
83. United States Steel Corporation. Atlas of isothermal transformation Diagrams: 1953 Supplement. 1953. https://books.google.com/books/about/Atlas_of_Isothermal_Transformation_Diagr.html?id=8aVTAAAAMAAJ. (accessed 2025-03-10)
84. Lundberg, S. M.; Lee, S. I. A unified approach to interpreting model predictions. *arXiv* **2017**, arXiv:1705.07874. Available online: https://doi.org/10.48550/arXiv.1705.07874. (accessed 10 Mar 2025)
85. Ravi, A. M.; Navarro-López, A.; Sietsma, J.; Santofimia, M. J. Influence of martensite/austenite interfaces on bainite formation in low-alloy steels below M_s. *Acta. Mater.* **2020**, *188*, 394–405. DOI
86. Tian, J.; Xu, G.; Zhou, M.; Hu, H.; Xue, Z. Effects of Al addition on bainite transformation and properties of high-strength carbide-free bainitic steels. *J. Iron. Steel. Res. Int.* **2019**, *26*, 846-55. DOI
87. Garcia-Mateo, C.; Caballero, F. G.; Bhadeshia, H. K. D. H. Acceleration of Low-temperature Bainite. *ISIJ. Int.* **2003**, *43*, 1821–5. DOI